




## EUROPEAN DATABASE FOR MULTISCALE MODELLING OF RADIATION DAMAGE

### ENTENTE

*This project has received funding from the Euratom research and training programme 2019/2020 under grant agreement No 900018*

#### **D4.5 Hybrid hardening models from SANS and NI experiments**


[M36] Aug 2023		Hybrid hardening models from SANS and NI experiments
Dissemination level	PU	
Lead Beneficiary	HZDR	
Lead Contributor	Frank Bergner (HZDR)	
Other contributors	Eberhard Altstadt (HZDR), Jann-Erik Brandenburg (HZDR), Paul Chekhonin (HZDR), Andreas Ulbricht (HZDR)	
Issue Date	30/08/2023	
Delay explanation		
WP leader review	Matti Lindroos	
Coordinator approval	Marta Serrano	

	<b>D4.5 Hybrid hardening models from SANS and NI experiments</b>	Page	2/38
		Rev	1
		Date	30/08/2023

## EXECUTIVE SUMMARY

In this ENTENTE deliverable, the results of two separated but related studies are reported. The first one describes hardening models and their application to predict the bulk-equivalent hardness of ion-irradiated layers of RPV steels from measured dependencies of the nanoindentation hardness on the contact depth. The models are based on the well-known Nix-Gao approach. The depth-dependent local hardness can be described as a deconvolution of the measured hardness integrating over the indentation plastic zone. Layer-substrate models and a layer-only model are considered and validated using nanoindentation data obtained for two RPV steels irradiated with Fe<sup>2+</sup> ions of 5 MeV energy. We have found that layer-substrate models are capable of resolving the bulk-equivalent hardness of the ion-irradiated layer, but suffer from limited transferability to the case of neutron-irradiated bulk materials. The reason are the implanted ions, which exhibit a peak between the depth of maximum displacement damage and the substrate. To overcome this issue, we propose a layer-only model exploiting experimental input that arises solely from a safe zone, where the implanted ions do not play a significant role. After conversion between bulk-equivalent hardness and Vickers (macro-) hardness, the results obtained for ion-irradiated layers and neutron-irradiated bulk samples give a consistent picture. In conclusion, a new quick methodology to predict irradiation hardening as function of exposure from nanoindentation tests on ion-irradiated samples has been introduced. Future studies are needed to consider the role of pile-up effects and tip-rounding effects on the accuracy of nanoindentation measurements at depths below 100 nm. The second study deals with a data compilation for neutron-irradiated RPV steels in the format of an Excel workbook called SANS-RPV. The data cover types and composition of RPV materials, initial microstructures and properties, irradiation conditions, and irradiation-induced changes of the microstructure and properties. The set of materials cover VVER-type RPV steels and welds, RPV reference and model steels distributed within an IAEA CRP, and PWR surveillance material from different sources. The data compilation also comprises metadata including references to published literature and reports. The original Excel workbook containing the data compilation can be found in an open access repository (Digital Object Identifier 10.14278/rodare.2441). In order to illustrate the use of the data compilation, several applications are considered in the deliverable. Examples are the comparison of cluster volume fractions derived from SANS and APT experiments, correlations of volume fraction and irradiation-induced property changes, and a comparison of the EONY embrittlement trend curve model with experimental data in terms of yield stress increase.




	<b>D4.5 Hybrid hardening models from SANS and NI experiments</b>	Page	3/38
		Rev	1
		Date	30/08/2023

## CONTENTS

<b>1</b>	<b>INTRODUCTION .....</b>	<b>4</b>
<b>2</b>	<b>HYBRID HARDENING MODELS FROM NANOINDENTATION EXPERIMENTS .....</b>	<b>5</b>
2.1	STATE OF THE ART OF THE ANALYSIS OF NANOINDENTATION DATA FOR ION-IRRADIATED LAYERS	5
2.2	NANOINDENTATION DATA FOR ION-IRRADIATED RPV STEELS.....	9
2.3	APPLICATION OF LAYER-SUBSTRATE MODELS OF IRRADIATION HARDENING.....	14
2.3.1	<i>Graded damage profile combined with original Nix-Gao law.....</i>	14
2.3.2	<i>Rectangular damage profile combined with generalized Nix-Gao law.....</i>	18
2.4	NEW LAYER-ONLY MODEL OF IRRADIATION HARDENING .....	20
2.5	TENTATIVE COMPARISON OF RESULTS FOR RPV STEELS IRRADIATED WITH IONS OR NEUTRONS ...	23
<b>3</b>	<b>HYBRID HARDENING MODELS FROM SANS EXPERIMENTS .....</b>	<b>24</b>
3.1	INTRODUCTION TO THE EXCEL WORKBOOK .....	24
3.2	SELECTED APPLICATIONS OF THE EXCEL WORKBOOK .....	25
3.2.1	<i>SANS versus APT.....</i>	25
3.2.2	<i>SANS-informed prediction of irradiation hardening.....</i>	27
3.2.3	<i>Volume fraction versus transition temperature shift.....</i>	31
3.2.4	<i>Predicted versus measured cluster characteristics .....</i>	32
3.2.5	<i>Embrittlement prediction and Trend Curves .....</i>	32
<b>4</b>	<b>CONCLUSIONS AND OUTLOOK.....</b>	<b>34</b>
<b>5</b>	<b>ACKNOWLEDGEMENT .....</b>	<b>35</b>
<b>6</b>	<b>REFERENCES .....</b>	<b>35</b>



	<b>D4.5 Hybrid hardening models from SANS and NI experiments</b>	Page	4/38
		Rev	1
		Date	30/08/2023

## 1 INTRODUCTION

The demonstration of the safety of nuclear installations, in particular the safety of reactor pressure vessels against brittle failure, relies to a large extent on the testing of surveillance samples. Irradiations in high-flux material test reactors also play an important role. However, the present period of nuclear fission energy production and research is characterized by a number of circumstances including:

- surveillance samples/material of existing nuclear installations being largely or fully consumed,
- shortage of available irradiation facilities and capacity,
- increasing number of nuclear installations having reached or being close to reach the design lifetime and the resulting request for lifetime extension to beyond 40 or 60 years,
- the development of new reactor concepts (e.g. Small modular reactors (SMRs) or Generation-IV reactors) posing new material challenges,
- increasing research needs related to the emergence of new promising material classes (e.g. Fe-Cr-Al alloys, high entropy alloys) and technologies (e.g. additive manufacturing).

Different research lines have been developed in response to these factors. These include:

- the optimized use of existing capacities for neutron irradiation,
- the optimized re-use of tested surveillance samples or samples irradiated in test reactors by way of small specimen test techniques (e.g. sub-sized fracture mechanics specimens, small punch testing),
- multiscale modelling linked with ongoing microstructure analyses on the  $\mu\text{m}$ - and  $\text{nm}$ -length scales,
- the use of ion irradiations to emulate neutron damage,
- the optimized re-analysis of the increasing amount of existing data.

The latter two research lines are addressed in the present deliverable.

The first part of the deliverable (Section 2) is dedicated to the combination of ion irradiation and nano-indentation (NI) in order to reveal characteristic features of the irradiation-induced hardening of materials. Major challenges are related to the small width of the ion-irradiated layers (of the order of  $1\ \mu\text{m}$ ), the damage gradient within the irradiated layers and the effect of the implanted ions. The final objective of the underlying work is to derive a bulk-equivalent hardness of the layer with best-possible transferability to the case of neutron-irradiated bulk samples. Even if this goal was not fully achieved, the nanoindentation hardness of ion-irradiated layers would still be an indicator of a material's irradiation resistance, which is of considerable importance in the stage of selection of a few candidate materials/conditions for nuclear applications from a rich base of available materials/conditions, i.e. so-called material screening. NI testing of ion-irradiated layers can be considered as a hot topic based on the frequency of publication. Therefore, the present study starts from a brief review of the state of the art. While results obtained for ion-irradiated pure Fe are shown to underpin the methodology of data analysis, two RPV steels, ANP-6 (RPV weld) and ANP-10 (RPV base metal forging), are in the centre of interest. The basic characterization of these materials, the experimental parameters and the test results adopted from WP-3 of ENTENTE are briefly summarized in order to facilitate readability of the deliverable. For the analysis of the NI data, two kinds of models are considered, namely two versions of a layer-substrate model and a layer-only model. The first version of the layer-substrate model combines a graded layer with the original Nix-Gao law, while the second version combines an effective homogeneous layer with a generalized Nix-Gao model. Both models suffer from the inherent impossibility to avoid the effect of the implanted ions, which do not appear in neutron-irradiated samples, in other words, they suffer from limited transferability to the case of neutron irradiation. However, they are still useful for the case that the characterization of the ion-irradiated layer is the ultimate objective of a study. The considered layer-only model potentially allows the effect of implanted ions to be avoided, though at the expense of other challenges. It is important to note that, once the irradiation-induced hardness increase of neutron-irradiated



	<b>D4.5 Hybrid hardening models from SANS and NI experiments</b>	Page	5/38
		Rev	1
		Date	30/08/2023

RPV steels is reasonably well predicted, there are strong correlations with neutron embrittlement (except for possible cases of non-hardening embrittlement).

The second part of the deliverable is dedicated to the implementation and application of a data compilation in the format of an Excel workbook called SANS-RPV. The overarching feature of SANS-RPV is the availability of results obtained by small-angle neutron scattering (SANS) for each of the covered neutron-irradiated RPV steels and irradiation conditions. Other quantities included are steel composition, initial microstructure, initial properties, irradiation conditions, characteristics of irradiation-induced nanostructures and irradiation-induced property changes. A handful of selected applications of the data compilation is considered explicitly, namely a comparison of SANS results with reported APT results, SANS-informed prediction of irradiation hardening, the correlation of volume fraction and transition temperature shift, reported prediction versus experimental volume fraction and the comparison of embrittlement trend curves with experimental data. These applications are rather illustrations on how the data compilation can be used instead of exhaustive case studies.

## 2 HYBRID HARDENING MODELS FROM NANOINDENTATION EXPERIMENTS

### 2.1 State of the Art of the Analysis of Nanoindentation Data for Ion-Irradiated Layers

Instrumented nanoindentation is a standardized method applied to characterize the hardness of a material (Oliver and Pharr 1992; 2004; Ruiz-Moreno et al. 2020; Standard DIN EN ISO 14577-1 2015). A pointed indenter (e.g. a three-sided pyramid Berkovich indenter) is pressed into the flat surface of an unirradiated or ion-irradiated sample. During the indentation process, load, displacement and stiffness are (quasi-) continuously recorded to calculate the contact depth  $h_c$  (of the indenter into the sample), the indentation hardness  $H_{IT}$  (load divided by projected contact area), and the indentation modulus  $E_{IT}$ . The numerous details involved in both the test method and the raw data analysis are addressed in the standard and the literature cited above. Here we assume that the dependence of the indentation hardness on the contact depth,  $H_{IT} = f(h_c)$ , is available as the result of a nanoindentation experiment performed for unirradiated and ion-irradiated samples of a material of interest. An example is shown in Figure 1 for illustration.

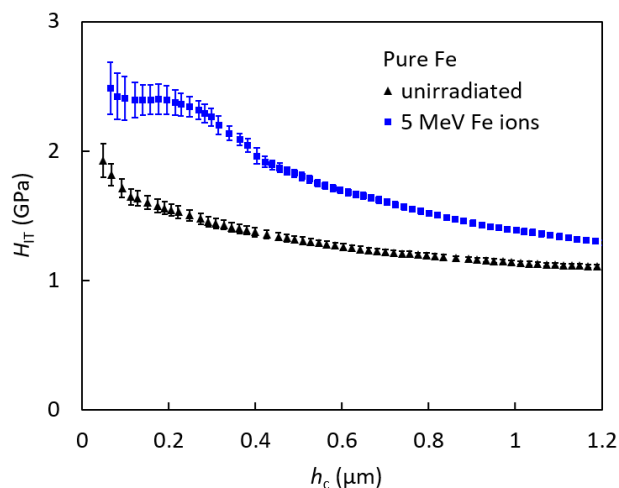


**Figure 1: Indentation hardness versus contact depth for unirradiated and ion-irradiated Fe.**

Figure 1 indicates a number of typical features:



	<b>D4.5 Hybrid hardening models from SANS and NI experiments</b>	Page	6/38
		Rev	1
		Date	30/08/2023

- The hardness of a homogeneous unirradiated sample increases at decreasing contact depth (“smaller is stronger”). This behaviour is called indentation size effect (ISE).
- Ion irradiation gives rise to an increase of hardness throughout the range of measurement.
- The irradiation-induced hardness increase as function of contact depth exhibits a peak.
- The hardness of the ion-irradiated sample asymptotically approaches the unirradiated hardness at large contact depths.
- The experimental error of the indentation hardness increases at decreasing contact depth.

It is important to emphasize that the hardness difference at a certain reference depth is an inadequate measure of the irradiation effect. This is because of a non-trivial coupling of the ISE with the irradiation effect. A careful consideration of the ISE is vital for meaningful conclusions to be drawn. Nix and Gao (1998) introduced a quantitative rationalization of the ISE based on the concept of geometrically necessary dislocations (GNDs). In brief, GNDs are formed in the material under the indenter tip in order to accommodate the shape changes enforced by the indentation process in an initially homogeneous sample. The density of GNDs,  $\rho_G$ , increases at decreasing indentation depth  $h$ , which gives rise to the mentioned increase of the hardness  $H$ . The Nix-Gao law assumes the following form:

$$\left(\frac{H}{H_0}\right)^2 = 1 + \frac{\rho_G}{\rho_S} = 1 + \frac{h^*}{h} \quad (1)$$

$\rho_S$  is the density of statistically stored dislocations (SSDs).  $H_0$  is the bulk-equivalent hardness, which the material would exhibit if only SSDs were present. For  $h \rightarrow \infty$ , it follows that  $H \rightarrow H_0$ , which justifies the term “bulk-equivalent” hardness. The following expression was derived for the characteristic length  $h^*$  (Nix and Gao 1998):

$$h^* = \frac{81}{2} b \alpha^2 \tan^2 \theta \left(\frac{G}{H_0}\right)^2 \quad (2)$$

$b$  and  $\alpha$  are the Burgers vector and the barrier strength of dislocations,  $G$  is the shear modulus of the material. The angle  $\theta$  is related to the indenter geometry with  $\tan \theta = 0.358$  for a Berkovich indenter.

If  $H^2$  is plotted as function of  $1/h$ , Eq. (1) represents a straight line, the intercept and slope of which allow the bulk-equivalent hardness and the characteristic length to be determined as illustrated in Figure 2.

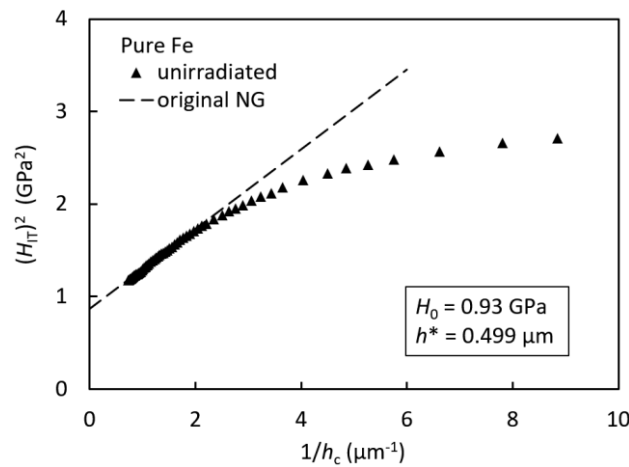


**Figure 2: Nix-Gao plot for unirradiated Fe to illustrate the determination of the bulk-equivalent hardness and the characteristic length according to Eq. (1).**



	<b>D4.5 Hybrid hardening models from SANS and NI experiments</b>	Page	7/38
		Rev	1
		Date	30/08/2023

While the straight line in Figure 2 provides a good fit of the experimental data in the range of  $1/h$  from 0.7 to  $2.2 \mu\text{m}^{-1}$ , that is the range of  $h$  from 0.5 to  $1.4 \mu\text{m}$ , there are systematic deviations at higher values of  $(1/h)$ , that means, smaller values of  $h$ . However, these smaller depths,  $h < 0.5 \mu\text{m}$ , are required to derive the ion-irradiation effect, as we will see more clearly later. It is therefore necessary to work out a more general description of the indentation hardness as function of contact depth.

Three factors were suggested to be potentially responsible for the deviations from the original Nix-Gao law:

- (1) Indentation is often accompanied by a pile-up or sink-in behavior of the material adjacent to the edges of the impression as demonstrated experimentally by way of atom force microscopy (Hardie, Roberts, and Bushby 2015; Zhu et al. 2022). Pile-up (or sink-in) results in corrections of both the projected contact area (and therefore per definition the hardness) and the contact depth. However, Zhu et al. (Zhu et al. 2022) reported that the pile-up corrections did not eliminate the curvature.
- (2) Tip rounding is also capable of producing a curvature (Zhu et al. 2022). This effect can be, at least partly, eliminated by way of properly calibrating the indenter area function.
- (3) In the original Nix-Gao model of the ISE, the density of GNDs diverges at decreasing indentation depth. This is unphysical because of the repulsive forces between individual dislocations. Several authors suggested generalizations of the Nix-Gao model by introducing a maximum allowable density of GNDs (Huang et al. 2006; Ruiz-Moreno and Hähner 2018; Haušild 2021).

While the first and second of these factors are mainly technical, the third one is fundamental and will be considered below.

Hähner suggested a generalization of Eq. (1) by introducing an exponential term (Frank Bergner et al. 2022):

$$\left(\frac{H}{H_0}\right)^2 = 1 + \frac{h^*}{h} \exp\left(-\frac{\bar{h}}{h}\right) \quad (3)$$

The additional length parameter  $\bar{h}$  in Eq. (3) is compatible with a maximum allowable density of GNDs. It is also important to note that the right-hand side of Eq. (3) passes a maximum at  $h = \bar{h}$ . The unphysical decrease following at larger values of  $1/h$  (smaller values of  $h$ ) is to be replaced by a constant corresponding to the peak value, as in Eq. (4):

$$\left(\frac{H}{H_0}\right)^2 = \begin{cases} 1 + \frac{h^*}{h} \exp\left(-\frac{\bar{h}}{h}\right) & (h \geq \bar{h}) \\ 1 + \frac{h^*}{e\bar{h}} & (h < \bar{h}) \end{cases} \quad (4)$$

For  $h \gg \bar{h}$ , Eq. (4) asymptotically approached the original Nix-Gao law, Eq. (1). Therefore, we will refer to Eq. (4) as the generalized Nix-Gao law (or equation, or model). A three-parameter fit (parameters  $H_0, h^*, \bar{h}$ ) to experimental data is illustrated in Figure 3. Most notably, Eq. (4) fits the experimental data in a much wider range than Eq. (1). In terms of the contact depth  $h$ , the range of good fit is extended from a lower limit of  $0.5 \mu\text{m}$  for Eq. (1) to a much smaller lower limit of  $0.12 \mu\text{m}$  for Eq. (4). This will turn out to be important for the analysis of ion-irradiated layers. It is also important to note that the best-fit values of  $H_0$  and  $h^*$  significantly differ from the respective values obtained before by applying the original Nix-Gao law, Eq. (1). As a consequence of the curvature, the bulk-equivalent hardness obtained from Eq. (4) is approximately 5% smaller than the corresponding value obtained from Eq. (1).



	<b>D4.5 Hybrid hardening models from SANS and NI experiments</b>	Page	8/38
		Rev	1
		Date	30/08/2023

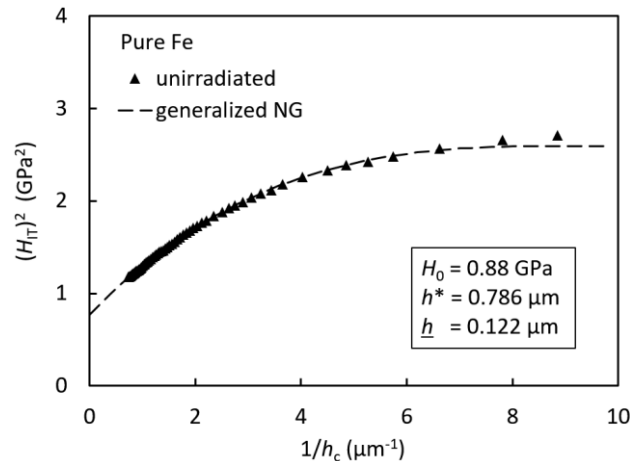


**Figure 3: Nix-Gao plot for unirradiated Fe to illustrate the fit of the generalized law according to Eq. (4).**

As a remarkable progress over classical hardness testing, instrumented nanoindentation paved the way to efficiently compare hardness values obtained for the same reference depth. Thus, by properly selecting the reference depth, a hardness difference between an ion-irradiated sample and an unirradiated reference sample became available (Robertson, Poissonnet, and Boulanger 1998) as an indicative measure of the ion-irradiation effect. Based on TEM, the same study also indicated interactions between irradiation-induced and indentation-induced microstructures. This kind of insight demonstrated the need to consider both the ISE and the concept of a bulk-equivalent hardness in order to derive a meaningful measure of the effect of ion irradiation on hardness.


Several attempts to derive the bulk-equivalent hardness of an ion-irradiated layer from nanoindentation tests have been (Kasada et al. 2011; Hosemann et al. 2012; Liu et al. 2014; Heintze et al. 2016; Kareer et al. 2018; Röder et al. 2018; Bonny et al. 2021). An early attempt that attracted attention relies on a change of slope in a bilinear fit of the squared indentation hardness as function of the inverse contact depth (Kasada et al. 2011; Liu et al. 2014; Heintze et al. 2016). Unfortunately, the bilinearity is disturbed by two effects. First, there is a broad transition between the (pseudo-) linear ranges due to the indentation plastic zone simultaneously containing parts of both the irradiated layer and the substrate. Second, the layer is typically in the depth range, where the systematic deviations from linearity mentioned above are important. It is therefore doubtful to infer the inflection point and the required straight-line parameters.

The first issue has been tackled by considering a layer-substrate system, assuming a hemispherical plastic zone (Johnson 1970), and applying a volume fraction model (Sargent 1979), the latter reflecting the fractions of the plastic zone belonging to the layer and the substrate. The parameterized model expression is then fitted to the experimental results allowing the bulk-equivalent hardness of the layer to be derived (Hosemann et al. 2012; Bonny et al. 2021). This approach was modified to take into account deviations from the hemispherical shape of the indentation plastic zone (Saleh et al. 2016), a graded damage profile of the layer (Xiao et al. 2017; Kareer et al. 2018; Röder et al. 2018; Das et al. 2022), a graded profile of implanted ions (Das et al. 2022), and deviations from the original Nix-Gao law (Frank Bergner et al. 2022) resulting from the maximum allowable density of GNDs.

All the models and approaches mentioned above have in common that they allow, within a certain degree of accuracy, the effect of ion-irradiation on the hardness to be extracted from nanoindentation measurements including indentation depths for which the indentation plastic zone reaches into the substrate. If the plastic





	<b>D4.5 Hybrid hardening models from SANS and NI experiments</b>	Page	9/38
		Rev	1
		Date	30/08/2023

zone reaches into the substrate, it necessarily also reaches into (or fully covers) the stopping range of the implanted ions. While the substrate effect is well considered within the layer-substrate models, the effect of the implanted ions are not properly accounted for. This raises serious questions about the transferability of the derived ion-irradiation-induced increase of the bulk-equivalent hardness (or any other parameter) to the case of neutron irradiation. Indeed, the injected interstitials were demonstrated to give rise to microstructures (e.g. so-called bands of loops) which do not form under neutron irradiation and, in this sense, represent artefacts.

## 2.2 Nanoindentation Data for Ion-Irradiated RPV Steels

The investigated materials are western-type generation-II/III RPV steels as introduced in ENTENTE Deliverable D3.1. ANP-6 is a weld exhibiting acicular ferrite structure and ANP-10 is a base metal (forging) with bainitic microstructure. SEM images of the typical microstructure in both materials are given in Figure 4.

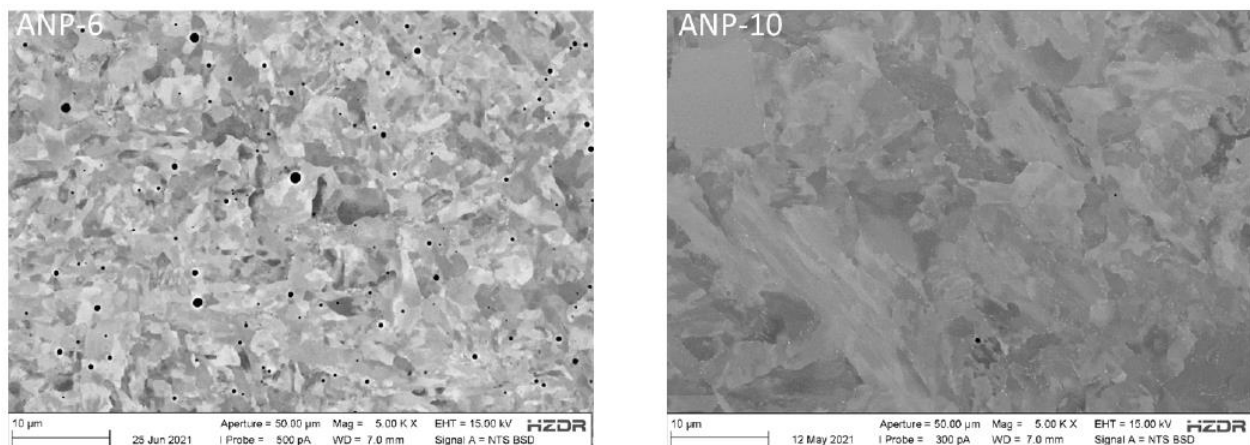


**Figure 4: Irradiated microstructure of ANP-6 and ANP-10**

Larger blocks of the materials in unirradiated state were provided by Framatome-Germany and small rectangular samples were cut from these blocks by electrical discharge machining. Mechanical sample preparation was done before irradiation treatment with the following steps:

- Grinding with SiC-paper down to 2500 grid,
- Mechanical polishing with 3µm and 1µm diamond paste,
- Fine-polishing with 60nm silica suspension (Mastermet, Buehler)

Initial trials included electro-polishing as a final preparation step, but undesirable surface damage was observed in the resulting sample surface. Comparison between electro-polished and mechanically fine-polished samples indicated no significant difference in the measured nanohardness (Figure 4). It was therefore decided to omit the electro-polishing step after mechanical fine-polish for all subsequently prepared samples. Self-ion irradiation treatment was conducted at the Ion Beam Center (IBC) at HZDR with the aim to achieve a radiation damages of 0.1 dpa and 1 dpa at 500 nm depth while keeping a zone directly below the surface free from injected interstitial atoms as much as possible. Based on the results of simulations using the software package “The Stopping and Range of Ions in Matter (SRIM)” by J.F. Ziegler the following irradiation parameters were chosen:

- Fe<sup>2+</sup>-ions accelerated to 5 MeV,
- Irradiation temperature 300 °C,



	<b>D4.5 Hybrid hardening models from SANS and NI experiments</b>	Page	10/38
		Rev	1
		Date	30/08/2023

- Beam current density 40 nA/cm<sup>2</sup>,
- Exposure time 0.6 h (0.1dpa at 500 nm) / 6 h (1 dpa at 500 nm),

The depth profiles of radiation damage and injected interstitial atoms for these conditions, as expected from the SRIM-calculations, are given in Figure 5.

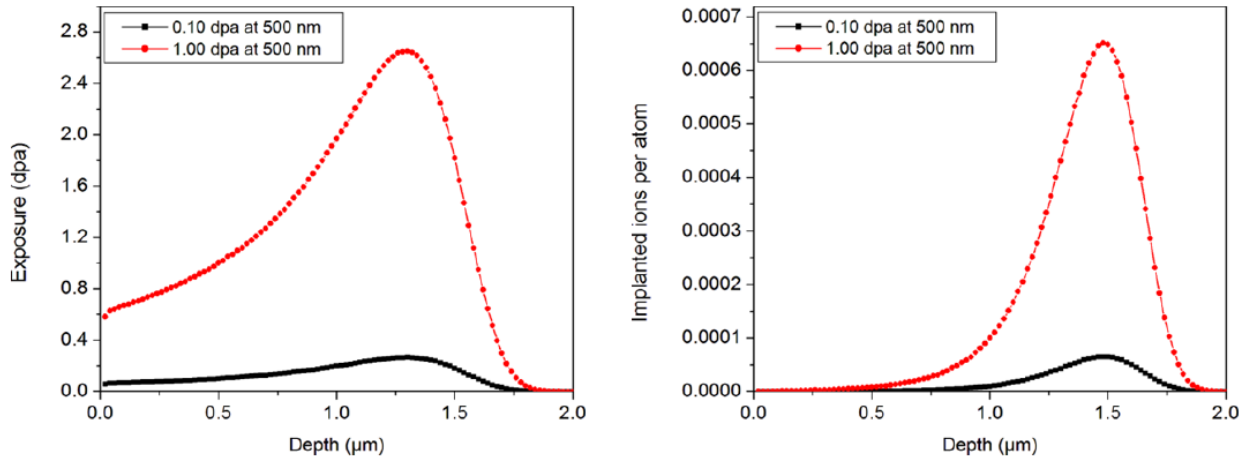


**Figure 5: Depth profiles of displacement damage (left) and implanted ions (right) from SRIM calculations.**

The indentation hardness of the irradiated and unirradiated samples was measured with an ASMEC UNAT nanoindenter (Figure 6) using the QCSM method (quasi-continuous stiffness measurement) to obtain depth-dependent information. All hardness measurements were done with the same Berkovich-geometry indenter tip. The contact area function of the tip and the device compliance were calibrated at the same time, using an automated method included in the UNATs device software. The method is based on measuring the elastic modulus of two different standard samples (here fused quartz and sapphire) and varying the calibration functions for contact area and device compliance until the correct elastic modulus for both materials is obtained.



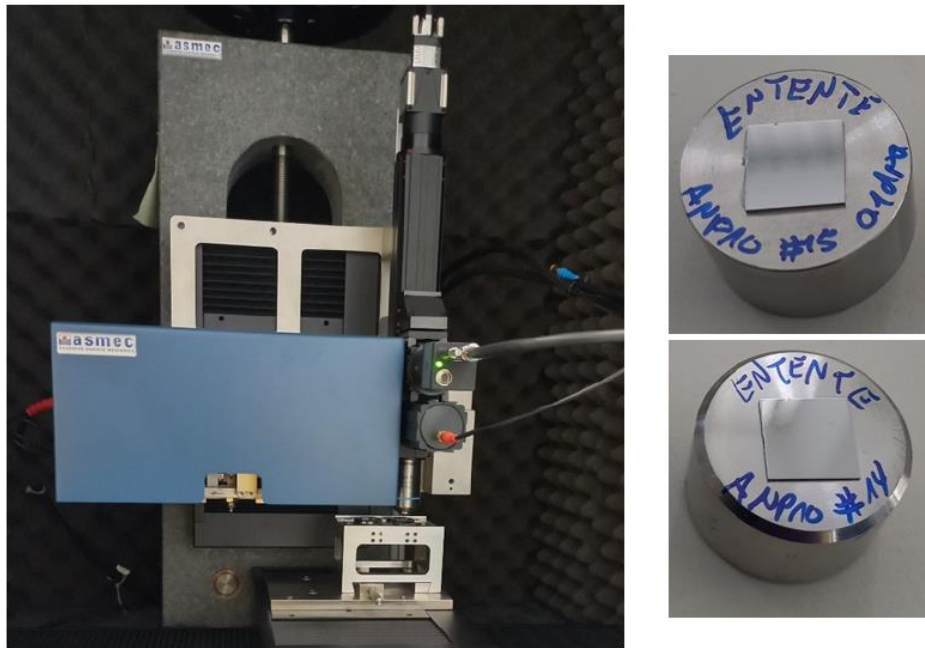


**Figure 6: Nanoindenter ASMEC UNAT and samples mounted for hardness testing.**

Figure 7 shows the applied loading scheme. After finding the sample surface, the load is increased quadratically to 50 mN over 250 s and kept constant for 20 s to monitor potential creep. Afterwards the sample is partially unloaded to 5mN and the load is kept constant again for drift correction before final unloading. During all segments, the nanoindenter is operated in load-controlled mode. Multiple hardness measurements were conducted for each sample and in a single run. Typically, 39 indentations + 3 approach points were done in a 6 x 7 array with 40  $\mu$ m spacing as shown in Figure 8.

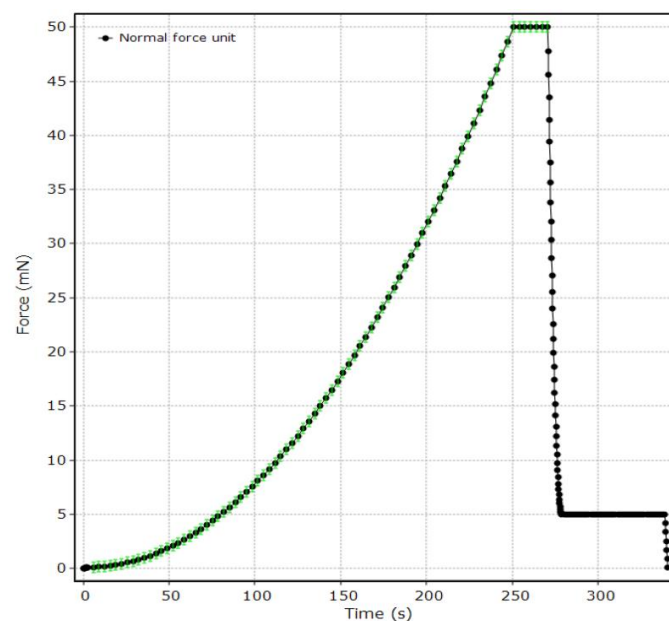


**Figure 7: Loading scheme for nanoindentation. Hardness measurement by QCSM at each point marked by green bars.**

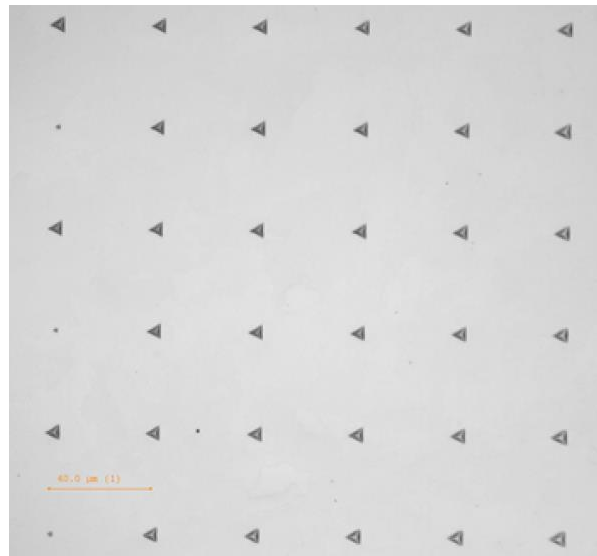


**Figure 8: Typical indentation array.**

The zero-point of contact between tip and sample surface during each indentation was determined by assuming Hertzian contact (i.e. loading exponent 3/2) for the first ~10 – 20 nm and fitting the beginning of the load displacement curves accordingly. Possible outliers were excluded manually. Drift correction was done based on the partially unloaded segment at the end of each indentation with the assumption that the average thermal drift rate during the whole indentation process is approximately constant. Typical load-displacement curves after these corrections are shown in Figure 9 (ANP-6) and Figure 10 (ANP-10). In general, the results showed good reproducibility with small deviation between individual curves.

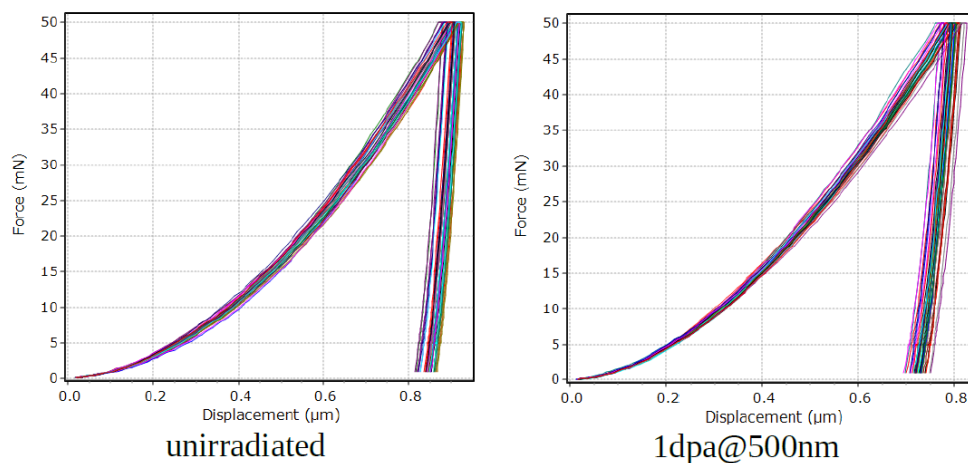


**Figure 9: Typical load – displacement curves for ANP-6.**

	<b>D4.5 Hybrid hardening models from SANS and NI experiments</b>	Page	13/38
		Rev	1
		Date	30/08/2023

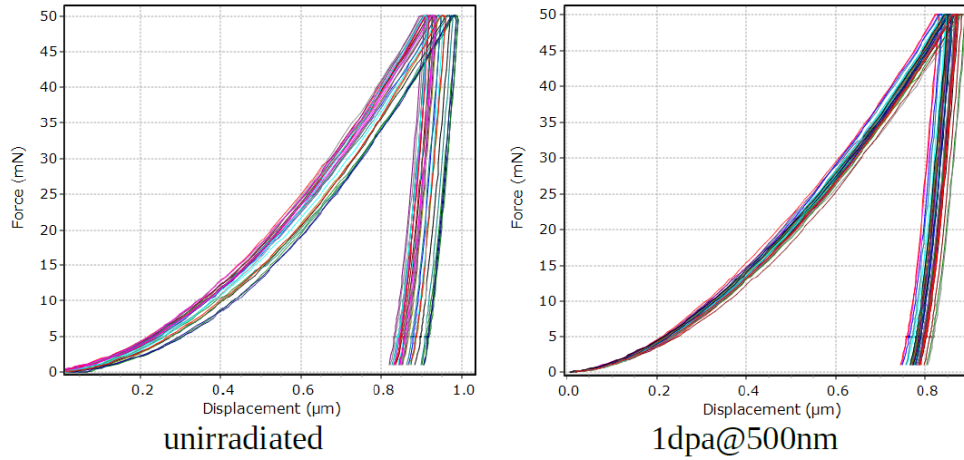


**Figure 10: Typical load – displacement curves for ANP-10.**

At each of the points marked by green bars in Figure 7, also the dynamic unloading stiffness  $S$  was measured according to the QCSM method by superposition of a small oscillation (8.5 Hz, 0.1 V amplitude for piezo oscillation at maximum load) to the indenter frame and monitoring of the resulting amplitudes in load and displacement. Indentation hardness  $H_{IT}$  and reduced elastic modulus  $E^*$  at each load  $F$  and corresponding indentation depth  $h$  can then be calculated as (Oliver and Pharr 1992; 2004; Ruiz-Moreno et al. 2020; Standard DIN EN ISO 14577-1 2015):

$$H_{IT} = \frac{F}{A(h_c)} \quad (5)$$

$$E_{IT}^* = \frac{\sqrt{\pi}}{2} \cdot \frac{S}{\sqrt{A(h_c)}} \quad (6)$$

$A(h_c)$  is the calibrated area function (projected area) and  $h_c$  the contact depth, i.e. the actual penetration depth of the indenter into the sample which differs from the measured indentation depth due to elastic deformation of the sample surface. Based on the unloading stiffness  $S$ ,  $h_c$  can be approximated as:

$$h_c = h - \epsilon \frac{F}{S} \quad (7)$$

with the geometry factor  $\epsilon = 0.75$  for a Berkovich indenter.

The measured indentation hardness as function of contact depth is plotted in Figure 11 and Figure 12 for the unirradiated and ion-irradiated conditions (0.1 dpa and 1 dpa) of ANP-6 and ANP-10, respectively. Post-irradiation annealed conditions also included in these plots will not be considered in the modelling part of the present deliverable. The data including statistical errors (including error propagation according to Eqs. (5) to (7)) are recorded and saved by the instrument firmware and transferred to suitable data analysis and graphics software suites.



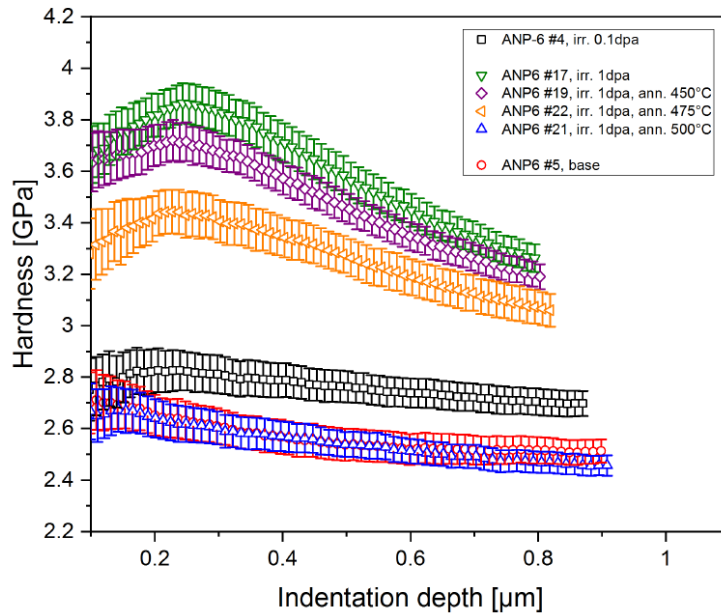


**Figure 11: Measured indentation hardness versus contact depth for ANP-6.**

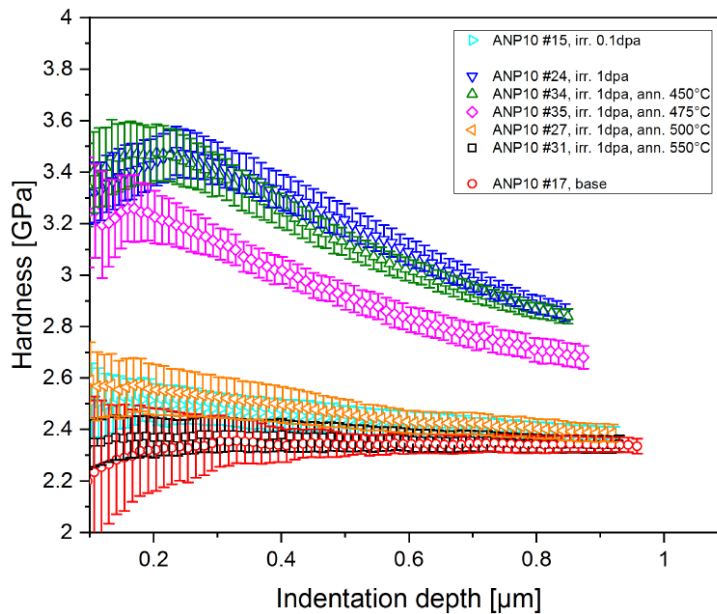


**Figure 12: Measured indentation hardness versus contact depth for ANP-10.**

## 2.3 Application of Layer-Substrate Models of Irradiation Hardening

### 2.3.1 Graded damage profile combined with original Nix-Gao law

The first version of a layer-substrate model applied in this deliverable is the model suggested by Röder et al. (Röder et al. 2018). The geometry of the problem is illustrated in Figure 13.



	<b>D4.5 Hybrid hardening models from SANS and NI experiments</b>	Page	15/38
		Rev	1
		Date	30/08/2023

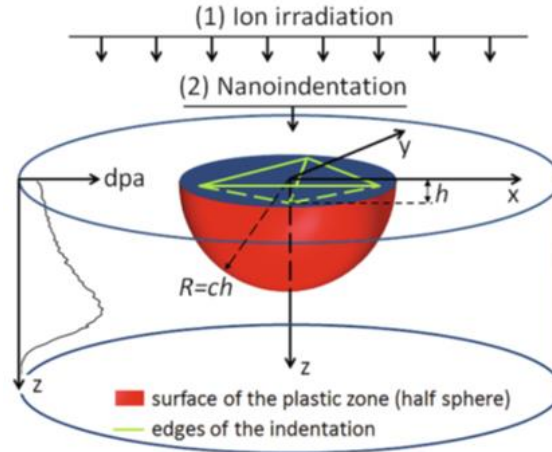


**Figure 13: Unirradiated ANP-6 sample to be supplied to CNRS for APT**

Starting point of the Röder model is the Nix-Gao law Eq. (1) applied to a homogeneous reference sample. To consider the inhomogeneous hardness distribution for an ion-irradiated sample, the following empirical model was developed: The profile of the local hardness  $H_0(z)$  is described as a function of the inhomogeneous dpa-profile  $\Phi(z)$ :

$$H_0(z) = H_s + \alpha[\Phi(z)]^n \quad (8)$$

A linear superposition of the hardness of the unirradiated substrate  $H_s$  with the irradiation induced hardness increase is assumed. To derive a relation between the depth-dependent actual hardness and the measured hardness for a given contact depth, we first have to average the actual hardness over the plastic zone. This kind of averaging is based on the volume law of mixture. The actual hardness profile  $H_0(z)$  averaged over a hemispheric plastic zone with radius  $R$  is considered as in Eq. (9). We assume this radius to be proportional to the contact depth  $R(h_c) = c \cdot h_c$ , with  $c$  as scale factor to be fitted to the experimental data. This factor determines the growth rate of the plastic zone during the indentation experiment. The hardness, which is averaged over the plastic zone given for a certain contact depth  $h_c$ , is taken as the mean hardness  $\langle H_0 \rangle$ :

$$\langle H_0 \rangle(h_c) = \frac{3}{2R(h_c)} \int_0^{R(h_c)} \left\{ 1 - \frac{z^2}{[R(h_c)]^2} \right\} H_0(z) dz \quad (9)$$

To further consider the indentation size effect, the Nix-Gao relation is modified by replacing the constant hardness,  $H_0$ , by the mean hardness profile  $\langle H_0 \rangle(h_c)$  as determined by Eq. (9). A constant characteristic length  $h^*$  is assumed, i.e. the dependence of  $h^*$  on the mean hardness is neglected, which is reasonable for small hardness changes. The indentation hardness is then described by:

$$H_{IT}(h_c) = \langle H_0 \rangle(h_c) \sqrt{1 + \frac{h^*}{h_c}} \quad (10)$$

Finally, the analytic model defined by Eqs. (8) to (10) is fitted to the experiment by way of variation of the parameters  $h^*$ ,  $s$ ,  $H_s$ ,  $\alpha$ , and  $n$  using a non-linear least-squares fitting routine implemented in Octave.

Plots of the experimental data obtained for the ENTENTE materials ANP-6 (left-hand side) and ANP-10 (right-hand side) are shown in Figure 14 along with the best-fit results according to the Röder model. The upper part of Figure 14 represents the measured  $H_{IT}$  versus  $h_c$  data and the corresponding best-fit curves, the middle part




shows the Nix-Gao plots of the same data, and the lower part indicates the dependence of the bulk-equivalent hardness of the ion-irradiated layer according to Eq. (8) as function of the distance  $z$  from the irradiated sample surface. We have found that the fit curves represent the experimental data well except for the smallest indentation depths. The best-fit parameters are listed in Table 1. This table also includes data reported in Röder et al. (2018) for the RPV steel ANP-4 (SOTERIA) for comparison.

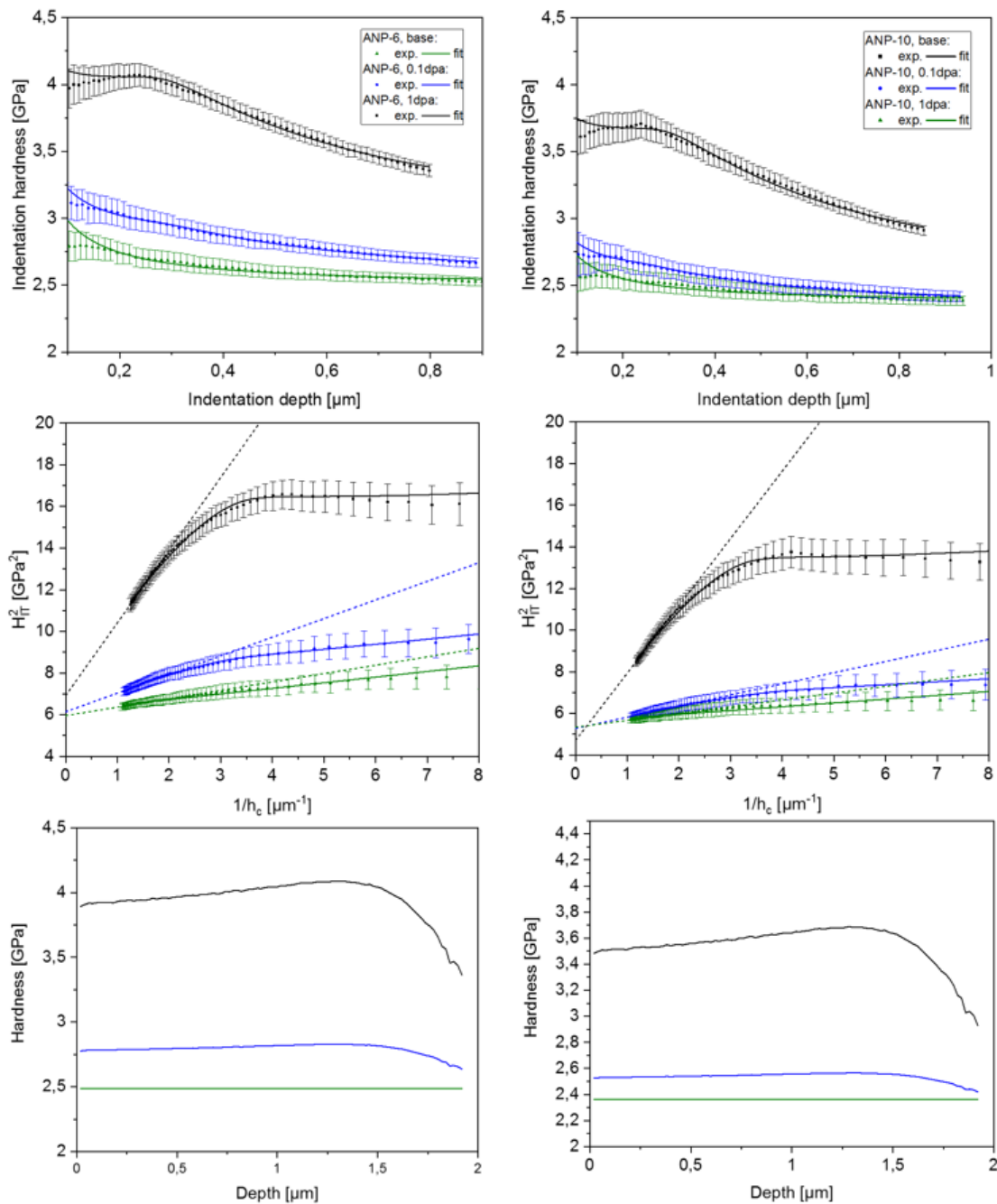


**Figure 14: Röder model applied to materials ANP-6 (left) and ANP-10 (right). Upper row – direct plots, middle row – Nix-Gao plots, lower row – depth profiles of bulk-equivalent hardness.**





	<b>D4.5 Hybrid hardening models from SANS and NI experiments</b>	Page	17/38
		Rev	1
		Date	30/08/2023

**Table 1: Best-fit parameters of the Röder model applied to the ENTENTE materials ANP-6 and ANP-10 and the SOTERIA material ANP-4.**

Material	Displacement damage (dpa)	$h^*$ (nm)	$H_0$ (GPa)	Factor $c$	Factor $\alpha$	Exponent $n$
ANP-6 (ENTENTE)	0	43	2.49	-	-	-
	0.1	34	2.85	6.7	0.39	0.02
	1	10	3.96	7.0	1.18	0.03
ANP-10 (ENTENTE)	0	33	2.36	-	-	-
	0.1	24	2.53	8.2	0.29	0.01
	1	15	3.55	6.8	1.23	0.06
ANP-4 (SOTERIA)	0	55	2.50	-	-	-
	0.1	29	3.25	6.9	0.93	0.04
	0.3	32	3.91	7.5	1.66	0.07
	1	29	4.43	8.1	2.08	0.09

The results summarized in Table 1 indicate that:

- The bulk-equivalent hardness  $H_0$  of the unirradiated RPV steels is similar.
- The bulk-equivalent hardness increases as function of displacement damage for each material.
- The characteristic length  $h^*$  tends to decrease as function of displacement damage.
- The factor  $c$  is approximately 7 to 8, that means, the radius of the indentation plastic zone is 7 to 8 times larger than the contact depth.
- The exponents  $n$  are small, which suggests a weak dependence of  $H_0$  on  $z$ , that means, an approximately rectangular damage profile.

All these findings are reasonable and render a tentative assessment of the ion-irradiation response possible.

However, both the quantitative accuracy of the results and the transferability of the results to the case of neutron irradiation are limited because of the following approximations involved in the model:

- The maximum allowable density of GNDs was not taken into account.
- The characteristic length  $h^*$  of the substrate and the whole layer are represented by a single value.
- A hemispherical shape of the indentation plastic zone is assumed as an approximation.
- The implanted ions are not considered.

Hence, an extension of the model is required in order to improve the accuracy. However, a direct extension of the Röder model, while conceptually possible, would increase the number of fit parameters to an unmanageable amount. It is therefore necessary to make a compromise. Taking into account the findings obtained for the application of the Röder model, the assumption of the generalized Nix-Gao law at the expense of an approximately rectangular damage profile would be a reasonable compromise.



	<b>D4.5 Hybrid hardening models from SANS and NI experiments</b>	Page	18/38
		Rev	1
		Date	30/08/2023

### 2.3.2 Rectangular damage profile combined with generalized Nix-Gao law

The second version of a layer-substrate model applied in this deliverable is the model reported by Bergner et al. (Frank Bergner et al. 2022). The dpa profile is approximated as an effective rectangular profile. The effect of the implanted ions is again neglected (or thought to be included in the effective rectangular profile). The model hardness  $H$  can then be expressed according to Eqs. (11) to (13):

$$H = f_i H_i + (1 - f_i) H_u \quad (11)$$

$$f_i = \begin{cases} 1 & \text{for } x \geq 1 \\ \frac{3}{2}x - \frac{1}{2}x^3 & \text{for } x < 1 \end{cases} \quad (12)$$

$$x = \frac{d_i}{c} \frac{1}{h} \quad (13)$$

In Eq. (11),  $H_u$  and  $H_i$  are the  $h$ -dependent hardness values according to Eq. (4) of the unirradiated substrate and the ion-irradiated layer, respectively. The weight factor  $f_i$  according to Eq. (12) is the volume fraction of the plastic zone occupied by the irradiated layer with  $x$  being the normalized inverse contact depth and  $d_i = 1.65 \mu\text{m}$  (for Fe ions of 5 MeV energy) being the effective thickness of the irradiated layer. The radius  $R$  of the hemispherical plastic zone is again taken as a multiple  $c$  of the contact depth  $h$ .

A two-step fit procedure is applied to calculate the parameters of interest. First, the expression according to Eq. (4) is fitted to the  $H_{IT} - h_c$  curve measured for the unirradiated reference sample. The resulting best-fit parameters are  $H_{0,u}$ ,  $h_u^*$  and  $\bar{h}_u$ . These parameters are treated as fixed in the fit of Eqs. (11) to (13) for the ion-irradiated sample. Moreover, we assume  $\bar{h}_i = \bar{h}_u$ , which is justified because of the relation with the maximum allowable density of GNDs. Therefore, the remaining free fit parameters are  $H_{0,i}$ ,  $h_i^*$  and  $c$ . We have fixed  $c = 7$ , which was found to give a smaller sum of square deviations than both  $c = 6$  and  $c = 8$ . To illustrate the result of the fit procedure, the same data set presented in Figure 1 to 3 for pure Fe is plotted in Figure 15. There is agreement between the experiment and the layer-substrate model prediction within the range of experimental errors. The parameters representative of the effective irradiated layer are given in green colour. The effective dpa value of the layer was calculated to be 1.36 dpa for the corresponding ion irradiation. The resulting irradiation-induced increase of the bulk-equivalent hardness,  $\Delta H_0$ , is 0.68 GPa.



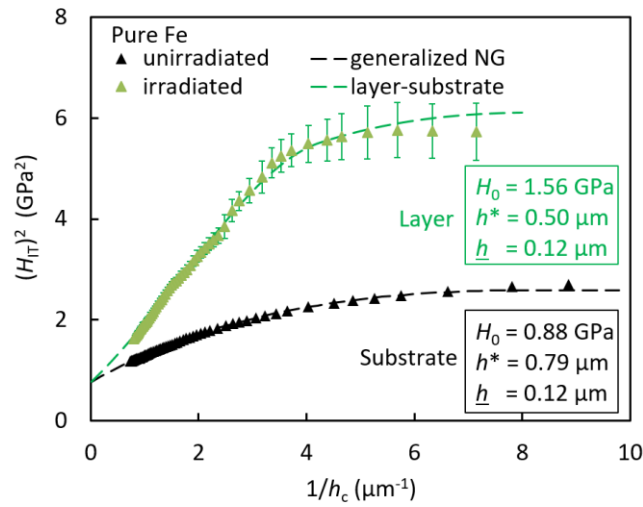



**Figure 15: Layer-substrate model applied to ion-irradiated pure Fe along with best-fit parameters.**

The least-squares fits to the measured  $H_{IT} - h_c$  data of ANP-6 and ANP-10 are summarized in Figure 16. The best-fit parameters are listed in Table 2.

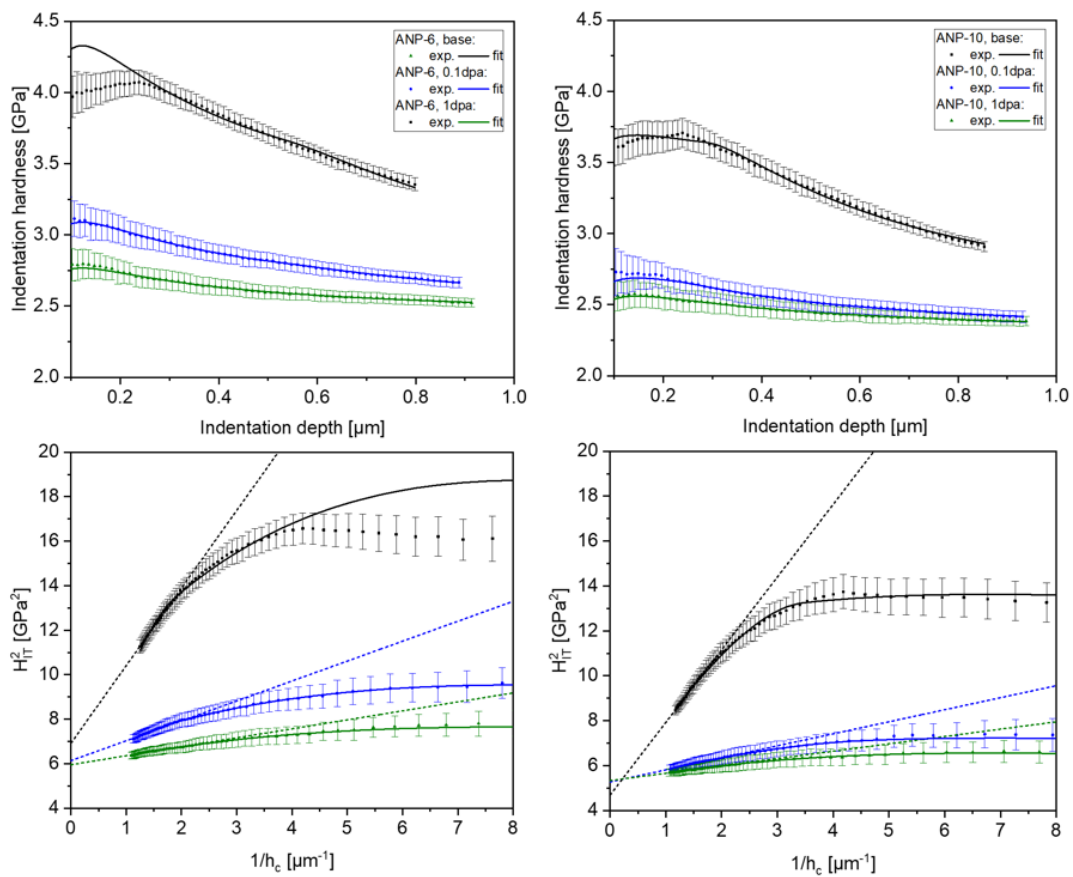


**Figure 16: Generalized Nix-Gao layer-substrate model applied to materials ANP-6 (left) and ANP-10 (right). Upper row – direct plots, lower row – Nix-Gao plots.**



	<b>D4.5 Hybrid hardening models from SANS and NI experiments</b>	Page	20/38
		Rev	1
		Date	30/08/2023

**Table 2: Best-fit parameters for the layer-substrate model with rectangular damage profile using the generalized Nix-Gao law.**

Material	Displacement damage (dpa)	$h^*$ (nm)	$\bar{h}$ (nm)	$H_0$ (GPa)	Factor $c$
ANP-6 (ENTENTE)	0	106	121	2.41	-
	0.1	179	121	2.48	3.2
	1	419	121	2.88	3.1
ANP-10 (ENTENTE)	0	108	147	2.27	-
	0.1	113	147	2.47	7.7
	1	78	147	3.68	5.8

The results obtained for ANP-6 are reasonable with respect to the trend of  $h^*$  to decrease and of  $H_0$  to increase at increasing neutron exposure. The factor  $c$  is in the expected range between 6 and 8. For ANP-6, the observed trends are questionable and  $c$  appears to be unreasonably small. This may be related to the systematic deviations between measurements and predictions at small indentation depths, see Figure 16.

Comparing the results listed in Table 1 (Röder model) and Table 2 (generalized Nix-Gao), that means two different models applied to the same data sets, the agreement is also reasonably good for ANP-10, but there are significant deviations for ANP-6. The most striking difference is the factor  $c$ , which is in the expected range for the Röder model. The questions raised above may be related to experimental factors which are not well understood so far and, therefore, not covered in the framework of the models.

## 2.4 New Layer-Only Model of Irradiation Hardening

As already concluded in Section 2.1 (State of the art), the layer-substrate models considered in the previous section have in common that the indentation plastic zone reaches into the substrate, and, therefore, necessarily also into the stopping range of ions, where irradiation-induced microstructures may fundamentally differ from any neutron-irradiated microstructure. Therefore, the results of the application of layer-substrate models may be representative of the ion-irradiated material itself, but suffer from questionable transferability to the case of neutron irradiation. Fortunately, there is a region between the sample surface and the stopping range of ions, where the concentration of implanted ions is negligibly small. This region is also called “safe zone” (Zinkle and Snead 2018).

We have identified two options to improve the transferability:

- A three-layer model, the first layer representing the safe zone, the second layer representing a region, where both the displacement damage and the concentration of implanted ions are significant, and the third layer representing the substrate. The model parameters determined for the first layer would then be free of implanted-ions artefacts.
- A single-layer model under the condition of a strongly limited range of contact depths for fitting such that the indentation plastic zone is fully contained in the safe zone. The challenge here is the need to extrapolate data obtained for a shallow near-surface range of contact depths to much larger (bulk) depths.



	<b>D4.5 Hybrid hardening models from SANS and NI experiments</b>	Page	21/38
		Rev	1
		Date	30/08/2023

As we do not currently feel prepared to handle the fit of a three-layer model, the present study is focussed on the second option, namely a single-layer (or layer-only) model.

The outline of the procedure is as follows:

- Fit Eq. (4) to the experimental data of the unirradiated reference, calculate  $H_{0,u}$ ,  $h_u^*$  and  $\bar{h}_u$ ,
- Use these data to derive approximate expressions for  $h_i^*$  and  $\bar{h}_i$ , which reduces the number of free parameters for the irradiated layer to only 1, namely  $H_{0,i}$ ,
- Solve Eq. (3) for  $H_{0,i}$ .
- Directly calculate  $H_{0,i}$  only taking into account the range of contact depths, for which the indentation plastic zone is fully contained in the safe zone.

As on the approximate expressions for  $h_i^*$  and  $\bar{h}_i$ , we use  $h_i^* = h_u^*$  as already applied above and take into account the inverse correlation between  $h^*$  and  $H_0^2$  implied by Eq. (2). This gives:  $h_i^* = h_u^* (H_{0,u}/H_{0,i})^2$ . Substituting these expressions in Eq. (3) and solving for  $H_{0,i}$  finally yields:

$$H_{0,i}(h) = \sqrt{H_i^2(h) - (h_u^* H_{0,u}^2) \frac{1}{h} \exp\left(-\frac{\bar{h}_u}{h}\right)} \quad (14)$$

Eq. (14) allows  $H_{0,i}$  to be directly calculated from the dependence of  $H_{IT}$  on  $h_c$  measured for the ion-irradiated material along with the parameters  $H_{0,u}$ ,  $h_u^*$  and  $\bar{h}_u$  calculated beforehand for the unirradiated reference. It is important to note that only a certain  $h_c$ -range is available for meaningful results to be obtained. The lower limit of this range is set to 0.1  $\mu\text{m}$ . On the one hand, this is because of the diverging errors of hardness measurement below 0.1  $\mu\text{m}$  indentation depth, which in turn are due to surface preparation issues, indenter tip rounding and similar experimental factors. On the other hand, the nearest-surface microstructure is affected by the operation of the free surface as sink for irradiation-induced point defects, which may give rise to another kind of transferability issue. The indentation plastic zone should at least reach deeply beyond this surface affected zone. The upper limit of the available  $h_c$ -range can be derived from the concentration profile of the implanted ions according to Figure 5. If we allow a maximum distance from the surface of 1  $\mu\text{m}$  (for 5 MeV ion energy) to largely avoid effects of the implanted ions and take into account a plastic zone extension factor  $c = 7$  (see above), an upper limit of the available  $h_c$ -range of  $1/7 = 0.14 \mu\text{m}$  is obtained. In summary, Eq. (14) is only applicable for the  $h_c$ -range from 0.10 to 0.14  $\mu\text{m}$ .

To illustrate the results for the pure Fe irradiated with 5 MeV Fe ions, we use the data plotted in Figure 1 and the parameters of the unirradiated reference given in Figure 3 to calculate the bulk-equivalent hardness of the ion-irradiated layer  $H_{0,i}$  according to Eq. (14). The resulting average value is 1.98 GPa. It is interesting to note that this value is higher than the corresponding result obtained from the generalized Nix-Gao layer-substrate model (1.56 GPa, see Figure 15). In order to better understand the reasons for this deviation, we reconsidered the generalized Nix-Gao layer-substrate model using the parameters derived from the application of the layer-only model. The results are shown in Figure 17.

Figure 17 is to be compared with Figure 15. It is found that, although the sum of square deviations for the data in green is higher in Figure 17 than in Figure 15, Figure 17 still shows a reasonably good fit except for the range of  $1/h_c$  close to 3 to 4  $\mu\text{m}^{-1}$  ( $h_c$ -range from 0.25 to 0.33  $\mu\text{m}$ ). This corresponds to extensions of the plastic zone up to depths  $z$  of 1.7 to 2.3  $\mu\text{m}$ , where the effect of the implanted ions is expected to be most pronounced. Hence, the excess hardness according to Figure 17 measured in this range may be attributed to the implanted ions. This insight may be considered as a point in favour of the layer-only model. Moreover, it indicates some lack of robustness of the layer-substrate model at least for the case of imperfect data. In any case, the result



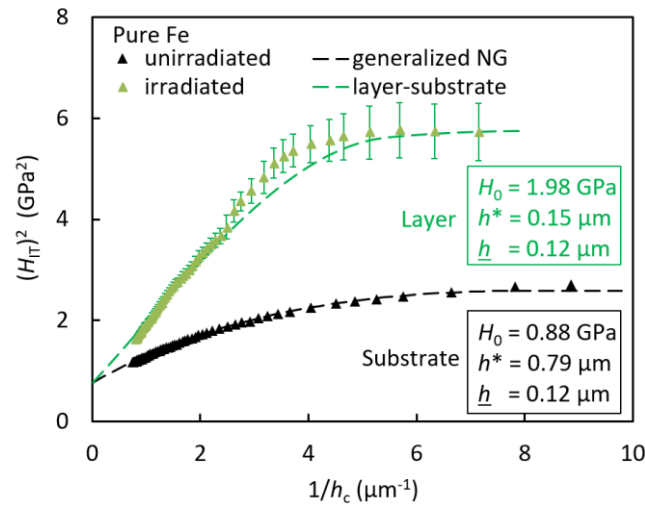


**Figure 17: Layer-substrate model applied to ion-irradiated pure Fe using the parameters derived from the layer-only model.**

obtained using the layer-only model cannot be significantly affected by the implanted ions. This is in contrast to any layer-substrate model and, therefore, lays the foundation for a better comparability with results obtained for neutron-irradiated material.


The experimental results obtained for ion-irradiated RPV steels indicate a behaviour at small indentation depths which is not well understood, but which is vital for meaningful modelling work. As a consequence, the results obtained using the layer-only model are to be considered as tentative. They are summarized in Table 3.

**Table 3: Bulk-equivalent hardness obtained for the layer-only model applied to ANP-6 and ANP-10, conversion into Vickers hardness increase and comparison with Vickers hardness increase measured for neutron-irradiated samples of ANP-6 and ANP-10.**

Particle type	Material	Dose (dpa)	Bulk-equivalent hardness, $H_0$ (GPa)	Hardness increase, $\Delta H_0$ (GPa)	Vickers hardness increase, $\Delta HV_{10}$
Ions	ANP-6	0	2.43	-	-
		0.1	2.78	0.35	32 *
		1	3.75	1.32	122 *
	ANP-10	0	2.29	-	-
		0.1	2.46	0.17	16 *
		1	3.44	1.15	106 *
Neutrons	ANP-6	0.08	-	-	98 **
	ANP-10	0.051	-	-	24 **

\* Conversion factor 92.4, \*\* as measured.



	<b>D4.5 Hybrid hardening models from SANS and NI experiments</b>	Page	23/38
		Rev	1
		Date	30/08/2023

The results in Table 3 show that the hardness increases as a function of dose for both materials. The hardness increase is smaller for ANP-10 as compared to ANP-6. The results obtained for the ion-irradiated materials will be compared with the measured neutron-induced increase of the Vickers hardness in the next section.

## 2.5 Tentative Comparison of Results for RPV Steels Irradiated with Ions or Neutrons

As a starting point, it is important to note that a number of ion-neutron transferability issues have been more or less exhaustively solved in the international context in recent years. These include:

- Technical ion-irradiation issues such as carbon contamination (countermeasures to minimize carbon contamination) (Was et al. 2017; Gigax et al. 2017; Malerba et al. 2021),
- Dose rate effect between ions and neutrons (temperature shift model) (Mansur 1978; Meslin, Radiguet, and Loyer-Prost 2013),
- Selection of test methods (nanoindentation, nanomechanical testing) (Hosemann et al. 2012),
- Consideration of the indentation size effect (Nix-Gao model, generalized Nix-Gao model).

The present study is focussed on an additional transferability issue, namely the effect of implanted ions. We have found that, at difference from other reported models, the layer-only model is a promising tool to avoid effects of implanted ions in ion-irradiated materials. However, this is still not the end of the story. For instance, it is well accepted that the use of the temperature shift model is not capable of correcting dose-rate effects on the simultaneous formation of different kinds of irradiation-induced nanostructures such as loops or solute-atom clusters. Any comparison of the irradiation-induced hardness increase derived for ion- and neutron-irradiated materials must therefore be treated as tentative.


Such a tentative comparison is provided in Table 3. For the ion-irradiated RPV steels, the measured bulk-equivalent hardness was converted into equivalent values of the Vickers hardness HV10 using an empirical conversion factor of 92.4. The irradiation-induced increase can then be compared with the as-measured increase of the Vickers hardness of the same steels irradiated with neutrons. We have found that ions and neutrons give rise to similar trends as function of fluence and material (ANP-6 versus ANP-10). However, reasonable quantitative agreement is not yet reached. This may be partly due to

- Experimental errors of the hardness for both ion- and neutron-irradiated steels,
- Approximations related to the concept of bulk-equivalent hardness applied to ion-irradiated steels,
- Different definitions of displacement damage for ion irradiations (e.g. from SRIM) and neutron irradiations (e.g. from NRT model),
- Remaining transferability issues, such as dose rate effects, not treated so far.

In conclusion, data for more materials/irradiation conditions are required in future to improve the statistics. At the same time, the mentioned remaining transferability issues have to be considered.

Finally, the irradiation-induced hardness increase is not the end of the story. The more relevant property from the viewpoint of reactor safety against brittle failure is irradiation embrittlement in terms of the brittle-ductile transition temperature shift. However, except for non-hardening embrittlement, hardening is the main reason of embrittlement. Therefore, correlations among the volume fraction of irradiation-induced precipitates, the increase of bulk-equivalent hardness (from nanoindentation), increase of Vickers hardness, yield stress increase and brittle-ductile transition temperature shift (or master curve  $T_0$  shift) are of particular interest (Nanstad et al. 2018). A tool to check the strength of such correlations based on a consistent data set will be introduced in the next section.



	<b>D4.5 Hybrid hardening models from SANS and NI experiments</b>	Page	24/38
		Rev	1
		Date	30/08/2023

## 3 HYBRID HARDENING MODELS FROM SANS EXPERIMENTS

### 3.1 Introduction to the Excel Workbook

The Excel workbook and data compilation in question, referred to as “SANS-RPV” below, is dedicated to the effect of neutron irradiation on the microstructure and mechanical properties of RPV steels. SANS-RPV differs from other data compilations or databases in form and content. The major difference, due to the original motivation of the data collection, consists in the fact that each individual data set was presupposed to include the results of small-angle neutron scattering (SANS) experiments aimed at deriving the volume fraction, number density, size distribution, and mean size of irradiation-induced clusters in neutron-irradiated RPV steels. All these microstructural data were obtained in a consistent way of carrying out SANS experiments and analyzing the results over a period of more than 30 years. The SANS samples of typical dimensions of 10 x 10 x 1 mm<sup>3</sup> were cut from broken halves of Charpy-type samples tested before. As another striking feature of SANS-RPV, the Vickers hardness HV10 was consistently measured after completion of the SANS experiments using the same sample and probing approximately the same macroscopic volume.

Historically, the data compilation significantly contributed to the insight that irradiation-induced hardening, yield stress increase, brittle-ductile transition temperature shift, and master curve  $T_0$  shift are correlated with the volume fraction  $f$  of irradiation-induced solute atom clusters of RPV steels, often most pronounced with  $\sqrt{f}$  (Böhmert, Viehrig, and Ulbricht 2004; Ulbricht, Böhmert, and Viehrig 2005; Ulbricht 2006). Simultaneously, the mean size of clusters was found to vary in a very narrow range (close to 1 nm in radius), which allowed to neglect effects of this factor for many applications. This insight was found to be sufficiently important to extend the data compilation and to establish SANS (volume fraction) as an efficient fingerprint indicator of neutron embrittlement. Based on the availability of corresponding material and mechanical property data mentioned above, it was consequential to develop SANS-RPV.


On the other hand, there are more comprehensive databases, such as MatDB, the Perform60 database, ASTM PLOTTER, or the database to be developed in ENTENTE WP2 to mention a few. Part of these databases may include results obtained from RPV embrittlement surveillance programs worldwide and/or unroll full database functionality. SANS-RPV does not compete with such databases. It is rather an easy-to-use Excel application containing a well manageable amount of unique (as outlined above) data with traceable reference to published original work. Selected applications will be outlined in Section 3.2. As an additional feature, SANS-RPV is freely accessible via the Rossendorf Data Repository (RODARE) including features such as ISBN, Open access, and version management to facilitate possible future extensions of the data collection.

As of now, the Excel workbook consists of three data spreadsheets, complemented by three corresponding metadata spreadsheets. The three data spreadsheets cover data for groups of RPV steels, namely VVER-type RPV steels, western-type RPV steels originating from the IAEA CRP “Optimizing Reactor Pressure Vessel Surveillance Programmes and their Analysis”, and western-type RPV steels reported by AREVA/FRAMATOME and EDF. Each data spreadsheet covers groups of data related to:

- RPV steel identification and type,
- Steel composition,
- Initial (unirradiated) microstructure,
- Initial (unirradiated) mechanical properties,
- Irradiation conditions,





	<b>D4.5 Hybrid hardening models from SANS and NI experiments</b>	Page	25/38
		Rev	1
		Date	30/08/2023

- Irradiated microstructure,
- Irradiated mechanical properties and irradiation-induced property changes.

The individual data are organized in vertical rows, the individual RPV steels and welds belonging to each group of steels are organized in horizontal rows. Some cells contain comments to indicate peculiarities or additional explanations related to specific data. The metadata spreadsheets cover additional information such as material producer, material provider, contact person if applicable, and references to published work or project reports, where more details can be found.

### 3.2 Selected Applications of the Excel Workbook

According to the original motivation and design of the SANS-RPV Excel Workbook, it is particularly useful for those applications for which the volume fraction of irradiation-induced solute clusters plays an important role. As cluster volume fraction and both hardening and embrittlement are known to exhibit pronounced correlations, there is a wide field of such applications. An example is the correlation between cluster volume fraction and irradiation-induced increase of Vickers hardness to be considered below. On the other hand, this means that non-hardening embrittlement, for which the cluster volume fraction is less relevant, is not the major domain of SANS-RPV.

Along with the results of SANS experiments, SANS-RPV also covers a multitude of other data such as composition, irradiation conditions, microstructure data, mechanical properties and their irradiation-induced changes. Correlations among these quantities are also of considerable interest. Below we summarize selected examples:

- Correlations among composition and property changes,
- Correlation between initial microstructure and yield stress (in terms of hardening mechanisms and superposition laws),
- Correlation between initial microstructure and yield stress increase (in terms of sink strength),
- Effects of neutron fluence on cluster volume fraction, hardening and embrittlement,
- Effects of other irradiation parameters such as neutron flux and temperature,
- Consistency of SANS volume fraction versus APT volume fraction,
- Correlation between hardness and yield stress,
- Correlations between hardening and embrittlement,
- Relationship between different measures of embrittlement such as  $\Delta T_{41}$  (from Charpy impact test) and  $\Delta T_0$  (from Master Curve testing).

This list can be easily extended. Selected examples will be considered in the subsections to follow. Here we wish to note that, using the logical operators of EXCEL, the potential applications listed above can also be discriminated with respect to special groups of RPV steels (e.g. weld versus base metal, low-Cu versus high-Cu RPV steels) or irradiation conditions (e.g. low versus high flux, irradiation temperature 255 °C versus 290 °C).

#### 3.2.1 SANS versus APT

In the first application case, the irradiation-induced solute clusters revealed by SANS and APT are compared. The applied SANS-RPV data subset covers all data sets from SANS-RPV for which SANS and APT data are simultaneously available. The cluster volume fractions inferred from APT experiments versus the cluster volume fractions derived from SANS assuming non-magnetic clusters are plotted in Figure 18.



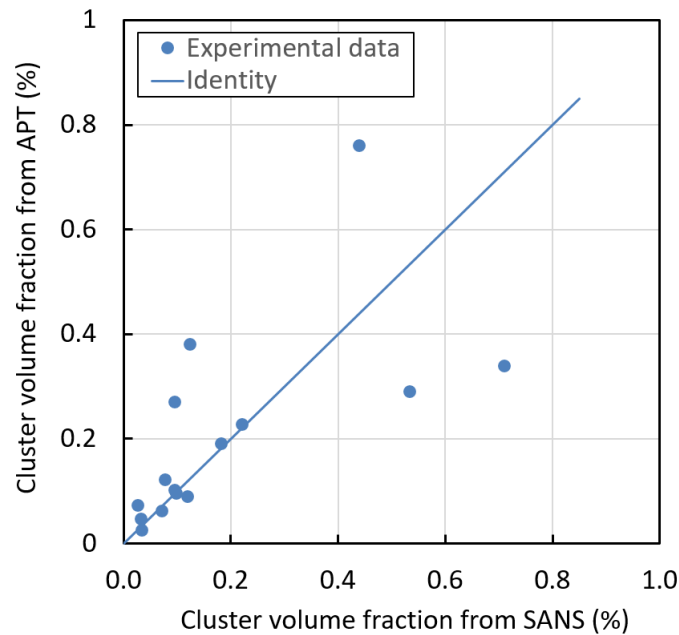


**Figure 18: APT cluster volume fraction versus SANS cluster volume fraction assuming non-magnetic clusters.**

Figure 18 shows that the volume fractions derived from SANS and APT approximately agree for most of the RPV steels. A few data points significantly deviate from the identity line. On average, the negative and positive deviations approximately cancel out, in other words, there is no bias of one method with respect to the other method. It is important to note that the SANS analysis was based on the assumption of non-magnetic clusters. If the clusters exhibited a non-zero magnetic moment, the resulting “corrected” volume fraction would be higher by a factor proportional to the square of the magnetic moment. This means that such a “correction” would introduce a bias (instead of removing an existing bias). In conclusion, the present data set is consistent with non-magnetic clusters on average. To further verify or qualify this conclusion, it would be important to consider the cases of pronounced deviation in more detail and to accumulate more data. The present data set is a valuable tool to advance in this direction.

A corresponding comparison is shown in Figure 19 in terms of cluster size. We have found a slight underestimation of the average cluster size derived from SANS as compared to APT. This underestimation is between 0 and 40%. It can be explained as a consequence of different method-specific ways to “see” clusters and to define size. For instance, the cluster–matrix interface is known to be graded. Therefore, there is a degree of arbitrariness in the position of the interface, and hence in the size estimation. Apart from this detail, the present set of size measurements based on SANS and APT is reasonably consistent.

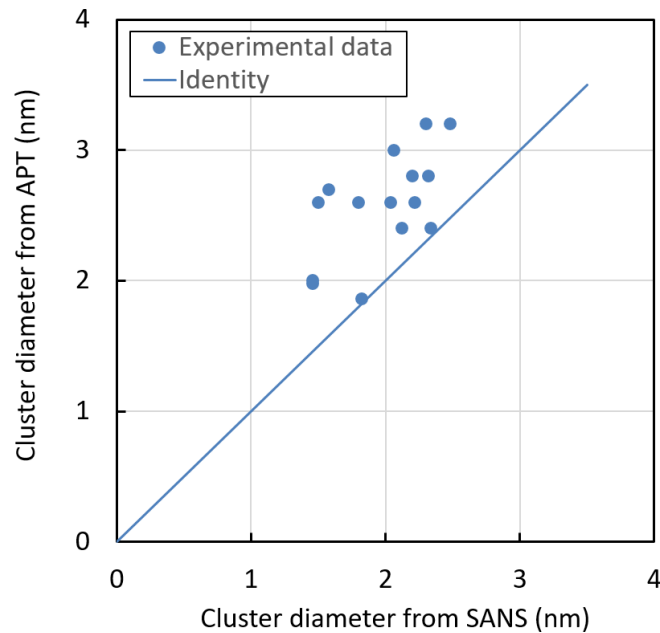


**Figure 19: APT cluster size versus SANS cluster size.**

The comparisons made above can be interpreted as an independent confirmation of the SANS results and, therefore, qualify the data for further meaningful statistical analyses and conclusions.

### 3.2.2 SANS-informed prediction of irradiation hardening

Irradiation hardening is typically treated in terms of the increases of Vickers hardness or yield stress. To address respective applications of the data collection we start from the correlation between the square root of the volume fraction of irradiation-induced solute clusters as extracted from SANS experiments and the irradiation-induced increase of the Vickers hardness HV10. A corresponding plot is shown in Figure 20. All materials and irradiation conditions covered by the data compilation are included in this plot without any exception. It is important to repeat that the Vickers hardness tests were performed after the SANS experiments using the same samples. Moreover, both methods, SANS and HV10, probe macroscopic volumes of the same order of magnitude of 10 mm<sup>3</sup>. Therefore, effects related to both the size of the probed volume (so-called size effects) and the material inhomogeneity can be excluded as major sources of deviations.

Figure 20 indicates a pronounced correlation between the square root of volume fraction  $f$  from SANS and the Vickers hardness increase  $\Delta HV10$ . It assumes the form:

$$\Delta HV10 = 1275\sqrt{f} \quad (15)$$

On the one hand, this confirms earlier reported insight based on the empirical treatment of smaller, more homogeneous groups of materials (Böhmert, Viehrig, and Ulbricht 2004; Ulbricht, Böhmert, and Viehrig 2005; Ulbricht 2006). Taking into account the weak variation of cluster size, Eq. (15) is also consistent with the dispersed barrier hardening (DBH) model. On the other hand, the correlation throughout different classes of RPV steels (including base metal and welds, Russian and western type RPV steels, low and high-Cu RPV steels, low and high-flux irradiations and so on) is a bit surprising or, in other words, the cases of larger deviations from the straight line in Figure 20 are not surprising. In any case, Eq. (15) does represent a reasonable and



	<b>D4.5 Hybrid hardening models from SANS and NI experiments</b>	Page	28/38
		Rev	1
		Date	30/08/2023

physically meaningful indication of the capability of irradiation-induced clusters to harden (and embrittle) RPV steels.

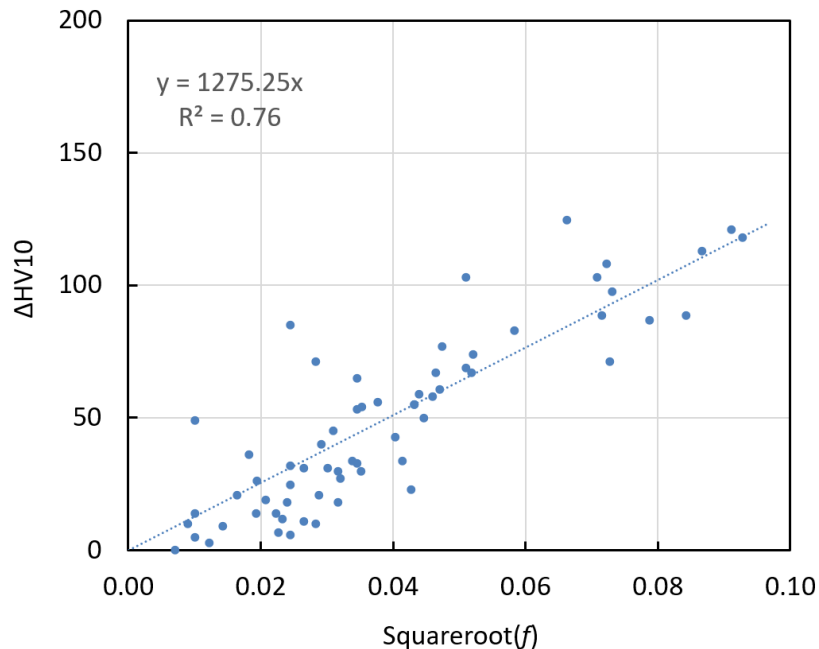


**Figure 20: Scatter plot of ΔHV10 and square root of volume fraction.**

A similar but physics-based application of the data collection was reported by Monnet (Monnet 2018). This author compared measured irradiation-induced increases of the yield stress and corresponding SANS-informed predictions using a multiscale modelling framework. The data were taken from the spreadsheet covering the IAEA RPV steels of a previous version of the present data collection SANS-RPV. [Note that the data sources were incorrectly cited in (Monnet 2018), the correct references are (Ulbricht, Böhmert, and Viehrig 2005; Ulbricht 2006; Zurbuchen, Viehrig, and Weiss 2009; Bergner, Ulbricht, and Viehrig 2009; Chaouadi 2012; Wagner 2017), see the metadata spreadsheet of the present version of SANS-RPV].

The type of calculations reported by Monnet (Monnet 2018) were repeated within the ENTENTE project (WP4) using essentially the same data set (there are a few minor differences in the data). Four versions of the SANS-informed prediction of irradiation hardening were covered:

- Classical dispersed-barrier hardening (DBH) model combined with linear superposition of hardening contributions,
- Classical DBH model combined with mixed (linear and square) superposition of hardening contributions,
- Monnet’s multiscale model combined with linear superposition of hardening contributions,
- Monnet’s multiscale model combined with mixed (linear and square) superposition of hardening contributions.

According to the classical DBH model (Seeger 1958), the yield stress  $\sigma_y$  arising from a dispersion of barriers is related to the number density and size of the dispersed barriers, here the irradiation-induced solute clusters (index s):



	<b>D4.5 Hybrid hardening models from SANS and NI experiments</b>	Page	29/38
		Rev	1
		Date	30/08/2023

$$\sigma_s = \alpha M G b \sqrt{N d} \quad (16)$$

$M$ ,  $G$ ,  $b$  and  $\alpha$  are the Taylor factor, the shear modulus, the Burgers vector of the dislocations and a factor of proportionality (related to the obstacle strength). Here we use  $M = 3.06$ ,  $G = 83$  GPa and  $b = 0.248$  nm, while  $\alpha$  is treated as a fit parameter.  $N$  and  $d$  denote number density and mean diameter of the solute clusters. This model was extended within a multiscale modelling framework and the resulting analytical expression was manipulated such that the analogy with Eq. (16) is emphasized (Monnet 2018):

$$\sigma_s = \left[ \frac{\Omega_{\text{obs}}}{\Omega_{\infty}} \cdot \frac{\ln(2\bar{D}/b)}{\ln(l/b)} \right]^{3/2} \frac{\ln(l/b)}{2\pi} M G b \sqrt{N d} \quad (17)$$

For the exact meaning of the symbols, we refer to (Monnet 2018).

In a real situation, the irradiation-induced solute clusters are not the only obstacles to dislocation glide. In particular, there are pre-existing obstacles such as grain boundaries (index  $g$ ), forest dislocations (index  $f$ ) and carbides (index  $c$ ). The most accepted way to superpose the contributions of forest dislocations, carbides and irradiation-induced obstacles is square superposition, while grain boundary (Hall-Petch) hardening adds linearly, resulting in the following expression for the irradiation-induced yield stress increase (Monnet 2018):

$$\Delta\sigma_y = \sigma_{y,\text{irr}} - \sigma_{y,\text{unirr}} = \sigma_g + \sqrt{\sigma_f^2 + \sigma_c^2 + \sigma_s^2} - \sigma_g - \sqrt{\sigma_f^2 + \sigma_c^2} = \sqrt{\sigma_f^2 + \sigma_c^2 + \sigma_s^2} - \sqrt{\sigma_f^2 + \sigma_c^2} \quad (18)$$

However, linear superposition is also occasionally applied and found to give reasonable results in some cases.

$$\Delta\sigma_y = \sigma_{y,\text{irr}} - \sigma_{y,\text{unirr}} = (\sigma_g + \sigma_f + \sigma_c + \sigma_s) - (\sigma_g + \sigma_f + \sigma_c) = \sigma_s \quad (19)$$

In order to apply Eq. (18), the knowledge of the the dislocation density and the size distribution of carbides or other particles is necessary. These data are available for selected cases (e.g. ANP-6 and ANP-10 within WP3 of ENTENTE), but, even though efforts are undertaken, typically not for the full set of RPV steels included in extended data collections such as SANS-RPV. It is therefore currently not feasible to estimate  $\Delta\sigma_y$  according to Eq. (18) for larger sets of RPV steels. Instead, we have calculated the required quantities according to Eqs. (20) and (21), taking into account that a full set of mean grain sizes  $d_g$  is available.

$$\sigma_f^2 + \sigma_c^2 = (\sigma_{y,\text{unirr}} - \sigma_g)^2 \quad (20)$$

$$\sigma_g = \alpha_g G \left( \frac{b}{d_g} \right) \quad (21)$$

We have used  $\alpha_g = 0.2$ . As introduced above, all four possible combinations of Eqs. (16) and (17) with Eqs. (18) and (19) were tested. The results are summarized in Figure 21.



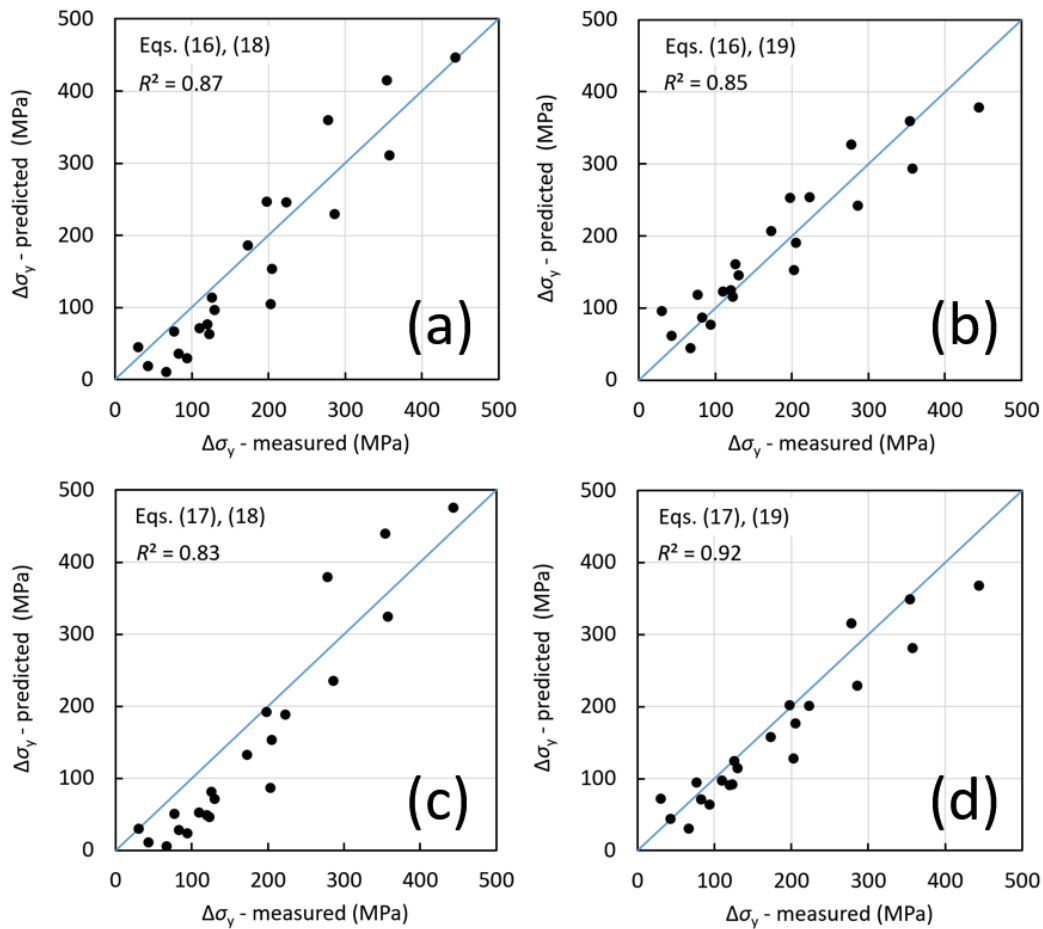


**Figure 21: Predicted versus measured yield stress increase for the IAEA subset of data from SANS-RPV. (a) Eqs. (16) and (18), (b) Eqs. (16) and (19), (c) Eqs. (17) and (18), (d) Eqs. (17) and (19).**

We have found that all four model versions give rise to reasonably good agreement between predicted and measured yield stress increase. However, the highest coefficient of correlation and the weakest trend of the residuals is observed for Monnet’s expression Eq. (17) combined with linear instead of mixed (linear and square) superposition. It is important to note that a best-fit value of the shear resistance of the obstacles  $\Omega_{obs} = 4.25$  GPa was obtained at difference from the original value of 4 GPa reported in (Monnet 2018). Monnet’s expression combined with mixed (linear and square) superposition results here in a weaker correlation and a trend of the residuals (underestimation at small  $\Delta\sigma_y$ , overestimation at large  $\Delta\sigma_y$ ). The classical DBH model was also found to be inferior, which confirms the advantage of Eq. (17) over Eq. (16). The reasons of this advantage are explained in detail in (Monnet 2018). The reasons why linear superposition seems to perform better than mixed superposition are complex. Foreman and Makin (Foreman and Makin 1967) demonstrated that the contributions of two families of weak obstacles (small obstacle strength or shear resistance) follow square superposition, while the contributions from a family of weak and a family of strong obstacles do not. In the latter case, the total effect depends on the relative number densities of the two families. If the number density of strong obstacles is much smaller than the number density of weak obstacles, the relatively few strong obstacles contribute more than expected from square superposition. Applied to RPV steels, the irradiation-induced solute clusters are much weaker obstacles than carbides and forest dislocations, but



	<b>D4.5 Hybrid hardening models from SANS and NI experiments</b>	Page	31/38
		Rev	1
		Date	30/08/2023

appear at a high number density. While these considerations may be part of the story, more work is required to ultimately solve the issue.

### 3.2.3 Volume fraction versus transition temperature shift

Irradiation hardening as considered in the previous section is not the quantity of highest priority. Its major importance arises from the correlation with embrittlement in terms of either brittle-ductile transition temperature shift or master curve  $T_0$  shift. These quantities are vital in the framework of demonstration of safety against brittle failure. It is therefore a logical step forward to consider the correlation of the volume fraction of irradiation-induced solute clusters with the transition temperature shift. This is done here in terms of  $\Delta T_{41}$ . We know from the previous section that  $\Delta HV_{10}$  is correlated with the square root of volume fraction. Furthermore,  $\Delta HV_{10}$  is also reported to be correlated with  $\Delta T_{41}$  (Nanstad et al. 2018). It is therefore reasonable to expect a correlation of the square root of volume fraction with  $\Delta T_{41}$  (Böhmert, Viehrig, and Ulbricht 2004; Ulbricht, Böhmert, and Viehrig 2005; Ulbricht 2006; Soneada et al. 2009). This kind of relationship is plotted in Figure 22 for VVER-type RPV steels included in SANS-RPV.

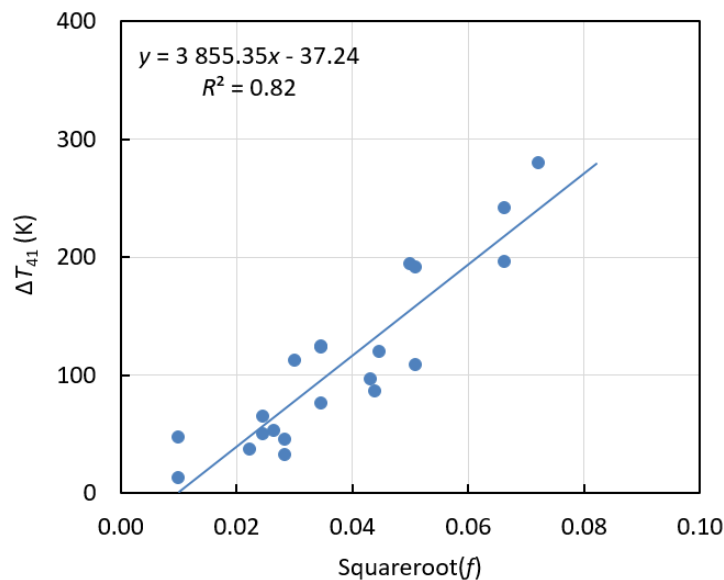


**Figure 22:  $\Delta T_{41}$  versus square root of volume fraction of irradiation-induced solute clusters in neutron-irradiated VVER-type RPV steels.**

While the correlation is strong, the intersection of the straight line with the axis is an unreasonable detail. Indeed, this intersection indicates that a non-zero volume fraction (say 0.01%) would not give rise to any embrittlement although it gives rise to hardening. Here it is important to note that the correlation according to Figure 22 does not take into account non-hardening embrittlement nor the reduction of the upper shelf energy. To explore the situation, Figure 23 shows a similar plot of  $\Delta T_{41}$  directly as a function of volume fraction (instead of its square root) for the same data set. We have found that the intersection with the axis is now positive, meaning that a zero volume fraction now can give rise to a non-zero transition temperature shift, which can be interpreted as either non-hardening embrittlement or hardening embrittlement due to nanostructures that give not rise to significant SANS (e.g. pure loops). The coefficient of correlation is also a bit higher. In conclusion, a linear relation between transition temperature shift and cluster volume fraction is a possible alternative to the reported square-root dependence (Böhmert, Viehrig, and Ulbricht 2004; Ulbricht,



	<b>D4.5 Hybrid hardening models from SANS and NI experiments</b>	Page	32/38
		Rev	1
		Date	30/08/2023

Böhmert, and Viehriq 2005; Ulbricht 2006; Soneada et al. 2009) at least for VVER-type RPV steels. This relation is specified in the text box of Figure 23. The confidence interval of the mean value of  $\Delta T_{41}$  and the expectation range for future estimates are graphically indicated.

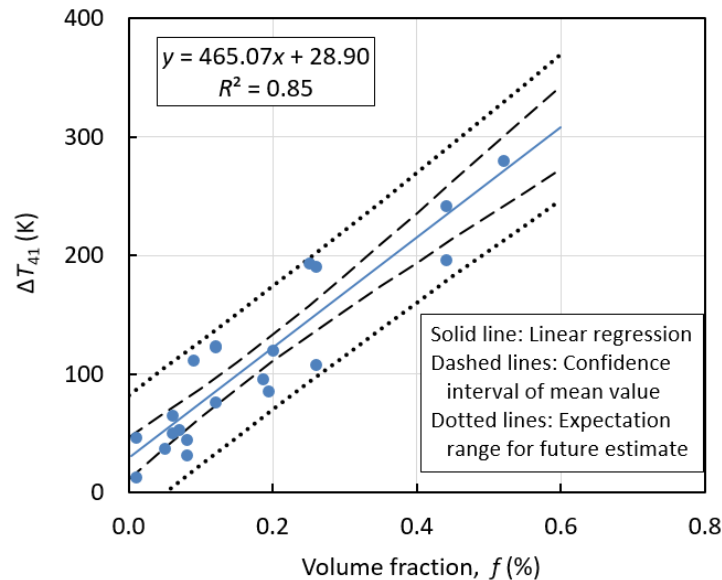


**Figure 23:  $\Delta T_{41}$  versus volume fraction of irradiation-induced solute clusters in neutron-irradiated VVER-type RPV steels.**

### 3.2.4 Predicted versus measured cluster characteristics

Castin and co-workers developed an object kinetic Monte Carlo (OKMC) model capable of predicting the size, volume fraction and number density of irradiation-induced solute clusters in RPV steels given their composition and irradiation conditions (Castin et al. 2020; 2022). To verify the model it was important to cross-check the calculations against experimentally determined sizes, volume fractions and number densities as done in the cited literature. Along with data obtained by means of atom probe tomography, part of the SANS data included in SANS-RPV were also used for this purpose. Without going into detail, the experimental results largely confirm the OKMC model predictions.

In a further step, Castin and co-workers linked the predicted cluster characteristics with the shift of the brittle-ductile transition temperature using physically based hardening models and empirical correlations (Castin et al. 2022). As shown in the previous sections of this deliverable, the SANS-RPV Excel workbook is well suited to contribute to the development, refinement and validation of such models and correlations. It is interesting to note that a square root dependence of the transition temperature shift on the cluster volume fraction was used in (Castin et al. 2022) as suggested before in the literature. However, as shown in section 3.2.3, a linear dependence on volume fraction instead of a square root dependence may be more appropriate in special cases.

### 3.2.5 Embrittlement prediction and Trend Curves

The Excel workbook presented in this deliverable is not particularly designed to assess different kinds of embrittlement trend curves (ETCs). Data bases and applications specialized on ETCs are available elsewhere. However, the input required to apply ETCs is also covered in the present workbook. It may therefore be fruitful





	<b>D4.5 Hybrid hardening models from SANS and NI experiments</b>	Page	33/38
		Rev	1
		Date	30/08/2023


to compare subsets of data included in the data collection with ETCs. As the amounts of both the data subsets and the reported ETC expressions and their combinations are huge, this can only be demonstrated here based on an example. We have selected the simplified EONY model according to Eqs. (7-2) to (7-5) in (Eason et al. 2006). Although it is focussed on embrittlement in terms of the transition temperature shift, the calculated shifts can be converted to yield stress increases. The resulting expressions were applied to the set of irradiation conditions of the RPV model steel IAEA-JPC included in SANS-RPV covering neutron irradiations in the VVER-2 prototype reactor at Rheinsberg/Germany (denoted RH) and the BR2 reactor at Mol/Belgium (Chaouadi 2012). The major difference of these two irradiation facilities is an irradiation temperature of 255 °C for RH and 290 °C for BR2. Moreover, the neutron flux for the RH irradiations ranges from 0.1 to 3.5 x 10<sup>12</sup> cm<sup>-2</sup> s<sup>-1</sup> (E > 1 MeV), whereas it ranges from 14 to 65 x 10<sup>12</sup> cm<sup>-2</sup> s<sup>-1</sup> (E > 1 MeV) for the BR2 irradiations (Chaouadi 2012). It is interesting to note that the irradiation temperature of the BR2 irradiations is more representative of currently operated PWR reactors, while the RH irradiations might be of relevance for certain future small modular reactors (SMRs).

Based on the composition, product form (plate) and irradiation conditions, the yield stress increase was calculated for the simplified EONY model and are compared with the measured values of the yield stress increase in Figure 24.

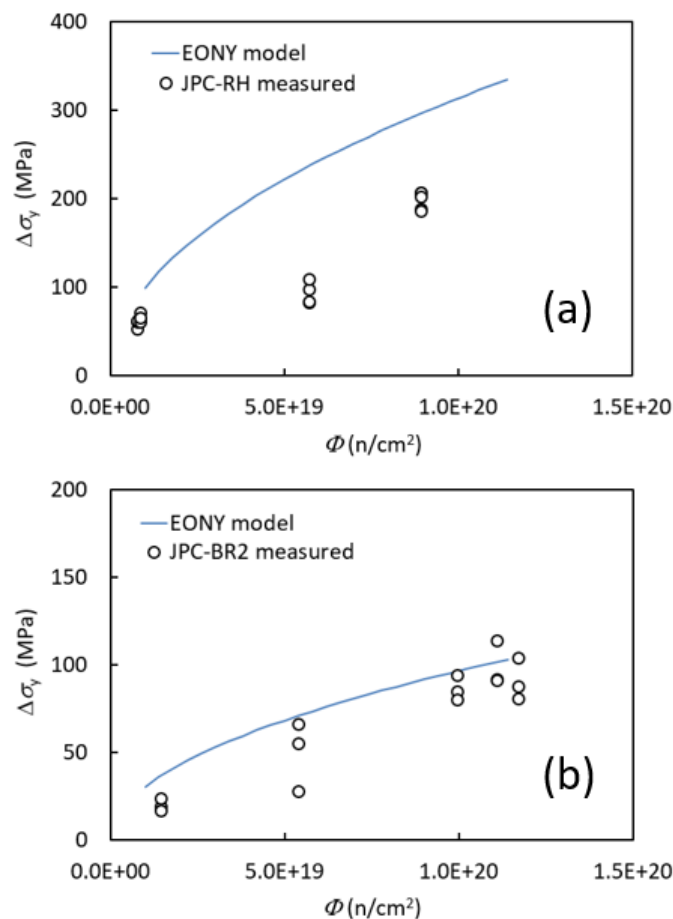


**Figure 24: EONY-type embrittlement trend curves (converted to yield stress increase) for material IAEA-JPC and comparison with experimental data, (a) Rheinsberg irradiation, (b) BR2 irradiation.**



	<b>D4.5 Hybrid hardening models from SANS and NI experiments</b>	Page	34/38
		Rev	1
		Date	30/08/2023

The trend curves indicate that the yield stress is expected to increase as function of the neutron fluence. In both cases, this yield stress increase per increment of fluence is smaller at higher fluences as indicated by the curvature. The yield stress increase “predicted” for the RH irradiations is higher than that for the BR2 irradiations, which is, within the EONY model, an effect of the lower irradiation temperature. As on the comparison with the experimental data, the EONY trend curve represents the data for the BR2 irradiation fairly well, it is conservative except for one data point, but not over-conservative. The experimental data might be better described by a linear dependence (straight line), but the trend-line curvature is not far from linear. For the RH irradiations, the “predicted” higher yield stress increase for the lower irradiation temperature is confirmed by the data. We have found an overestimation of the trend curve (towards the conservative side) and a more pronounced discrepancy between the curvatures. Indeed, at difference from the trend curve, the data even suggest a higher yield stress increase per increment of fluence at higher neutron fluence [Bergner 2009]. It can only be speculated here that the different behaviours of the RH and BR2 irradiations would be mainly due to the different irradiation temperatures and to the different flux ranges. Some unidentified material inhomogeneity between the samples irradiated up to medium or high fluence might also contribute. Instead, the reasonably small scatter of the experimental data points indicate that experimental errors are not an obvious factor to explain the curvature.


## 4 CONCLUSIONS AND OUTLOOK

The studies and implementations presented in this deliverable are dedicated to the nanoindentation-informed prediction of the bulk-equivalent hardness of ion-irradiated layers (Section 2) and the SANS-informed prediction of neutron-irradiation-induced hardening and embrittlement of RPV steels (Section 3).

It was demonstrated that the bulk-equivalent hardness of ion-irradiated layers can be reasonably well predicted on the basis of substrate-layer models. While the respective estimates of the bulk-equivalent hardness are representative of the ion-irradiated layer (including damage profiles and implanted ions), they suffer from limited transferability to the case of neutron-irradiated materials. To overcome this issue, we have suggested a layer-only model based on a generalized version of the Nix-Gao model of the indentation size effect. This model is conceptually capable of resolving the issue of the implanted ions by limiting the range of contact depths to within a safe zone. A critical comparison of the bulk-equivalent hardness of the ion-irradiated layer with results derived from Vickers hardness testing of neutron-irradiated counterparts indicates reasonable consistency. The question of accuracy and precision of measurements at indentation depths below 100 nm is vital for the application of a layer-only model. This requires further efforts including the consideration of pile-up corrections and tip-rounding effects. An alternative option is the increase of the ion energy to beyond 10 MeV in order to widen the safe zone towards larger indentation depths.

A data compilation on RPV steels in the format of an Excel workbook, called SANS-RPV, is introduced in Section 3. SANS-RPV covers the material type, composition, initial microstructure, initial properties, neutron-irradiation conditions, irradiation-induced microstructures, and irradiation-induced property changes; it incorporates VVER-type RPV steels and welds from different sources, reference/model RPV steels and welds distributed within an IAEA Co-ordinated Research Programme, and PWR-type RPV steels and welds investigated within past and running European and national projects. A unique feature of the data compilation (as compared to other databases) is the availability of consistent sets of SANS data for all materials/irradiation conditions. SANS RPV also covers metadata including references to published work, where the data were originally reported. In order to illustrate the benefit of the data compilation, selected applications out of the manifold potential applications are introduced and their implications are discussed. The following questions are addressed within the selected applications:



	<b>D4.5 Hybrid hardening models from SANS and NI experiments</b>	Page	35/38
		Rev	1
		Date	30/08/2023

- Volume fraction and size of solute clusters derived from SANS versus APT: On average, there is no bias of volume fractions of solute clusters derived from SANS indicating negligible average magnetic moments of the clusters.
- The correlation of cluster volume fraction and irradiation-induced yield-stress increase: Against the dominating view, linear superposition seems to perform better than mixed superposition in the considered case.
- The correlation of cluster volume fraction and transition temperature shift: For VVER-type RPV steels investigated, a linear correlation of the transition temperature shift with the volume fraction seems to perform better than the reported correlation with the square root of volume fraction.
- Cluster volume fraction and size derived from SANS may be useful to validate an OKMC model capable of predicting volume fraction, number density and size of clusters.
- The data compilation may also be applied to assess Embrittlement Trend Curve models.

The data compilation is available via an open access repository using the Digital Object Identifier 10.14278/rodare.2441. Application of the data compilation and communication of issues are encouraged.


## 5 ACKNOWLEDGEMENT

Numerous former and current colleagues and partners contributed to this deliverable. This is particularly applicable to the data compilation introduced in Section 3. We would like to mention and acknowledge contributions, including testing, analysis and supply of samples or data, by Hans-Werner Viehrig, Holger Richter, Conrad Zurbuchen, Kanwer Singh Arora, Arne Wagner (all formerly with HZDR), Hieronymus Hein (Framatome Erlangen), Bertrand Radiguet (CNRS/University Rouen), Rachid Chaouadi (SCK·CEN), Patrick Todeschini (EDF), Marta Serrano (CIEMAT), Ferenc Gillemot (EK-CER) and former colleagues from RRC Kurchatov. Elvira Oñorbe Esparraguera (CIEMAT) implemented several Embrittlement Trend Curve models including the EONY model applied in Section 3.2.5 of this deliverable, many thanks for that. Thanks to Mark Kirk, who draw our attention to a numerical error in a previous version of SANS-RPV. Last but not least, microstructure characterization and mechanical testing of neutron-irradiated samples is based on the machining, preparation and handling of radioactive samples. We would like to express our gratitude to the former and current technicians at HZDR: Mario Houska, Gudrun Müller, Jens Pietzsch, Vanessa Reinke, Henry Richter, Toni Richter, Michaela Rossner, Ulrich Skorupa, Wolfgang Webersinke and Tilo Welz.

## 6 REFERENCES


- Bergner, F., A. Ulbricht, and H. -W. Viehrig. 2009. “Acceleration of Irradiation Hardening of Low-Copper Reactor Pressure Vessel Steel Observed by Means of SANS and Tensile Testing.” *Philosophical Magazine* 89 (12): 795–805. <https://doi.org/10.1080/09500830903304117>.
- Bergner, Frank, Cornelia Kaden, Aniruddh Das, Susana Merino, Gonzalo Diego, and Peter Hähner. 2022. “Nanoindentation Applied to Ion-Irradiated and Neutron-Irradiated Fe-9Cr and Fe-9Cr-NiSiP Model Alloys.” *Journal of Applied Physics* 132 (4): 045101. <https://doi.org/10.1063/5.0098807>.
- Böhmert, J, H.-W Viehrig, and A Ulbricht. 2004. “Correlation between Irradiation-Induced Changes of Microstructural Parameters and Mechanical Properties of RPV Steels.” *Journal of Nuclear Materials* 334 (1): 71–78. <https://doi.org/10.1016/j.jnucmat.2004.05.003>.
- Bonny, G., T. Khvan, A. Bakaeva, C. Yin, A. Dubinko, C. Cabet, M. Loyer-Prost, N. Castin, A. Bakaev, and D. Terentyev. 2021. “Effect of Statistically Stored Dislocations in Tungsten on



	<b>D4.5 Hybrid hardening models from SANS and NI experiments</b>	Page	36/38
		Rev	1
		Date	30/08/2023


- the Irradiation Induced Nano-Hardening Analyzed by Different Methods.” *Journal of Nuclear Materials* 543: 152543. <https://doi.org/10.1016/j.jnucmat.2020.152543>.
- Castin, N., G. Bonny, A. Bakaev, F. Bergner, C. Domain, J.M. Hyde, L. Messina, B. Radiguet, and L. Malerba. 2020. “The Dominant Mechanisms for the Formation of Solute-Rich Clusters in Low-Cu Steels under Irradiation.” *Materials Today Energy* 17 (September): 100472. <https://doi.org/10.1016/j.mtener.2020.100472>.
- Castin, N., G. Bonny, M.J. Konstantinović, A. Bakaev, F. Bergner, C. Courilleau, C. Domain, et al. 2022. “Multiscale Modelling in Nuclear Ferritic Steels: From Nano-Sized Defects to Embrittlement.” *Materials Today Physics* 27 (October): 100802. <https://doi.org/10.1016/j.mtphys.2022.100802>.
- Chaouadi, R. 2012. “Irradiation Effects on the Tensile Properties of LONGLIFE Materials Irradiated in the BR2.” External Report SCK.CEN-ER-191. SCK.CEN Mol, Belgium.
- Das, Aniruddh, Eberhard Altstadt, Cornelia Kaden, Garima Kapoor, Shavkat Akhmadaliev, and Frank Bergner. 2022. “Nanoindentation Response of Ion-Irradiated Fe, Fe-Cr Alloys and Ferritic-Martensitic Steel Eurofer 97: The Effect of Ion Energy.” *Frontiers in Materials* 8 (January): 811851. <https://doi.org/10.3389/fmats.2021.811851>.
- Eason, E.D., G.R. Odette, R.K. Nanstad, and T. Yamamoto. 2006. “A Physically Based Correlation of Irradiation-Induced Transition Temperature Shifts for RPV Steels.” Report ORNL/TM-2006/530. Oak Ridge National Laboratory, Oak Ridge, Tennessee.
- Foreman, A. J. E., and M. J. Makin. 1967. “Dislocation Movement through Random Arrays of Obstacles.” *Canadian Journal of Physics* 45 (2): 511–17. <https://doi.org/10.1139/p67-044>.
- Gigax, Jonathan G., Hyosim Kim, Eda Aydogan, Frank A. Garner, Stu Maloy, and Lin Shao. 2017. “Beam-Contamination-Induced Compositional Alteration and Its Neutron-Atypical Consequences in Ion Simulation of Neutron-Induced Void Swelling.” *Materials Research Letters* 5 (7): 478–85. <https://doi.org/10.1080/21663831.2017.1323808>.
- Hardie, Christopher D., Steve G. Roberts, and Andy J. Bushby. 2015. “Understanding the Effects of Ion Irradiation Using Nanoindentation Techniques.” *Journal of Nuclear Materials* 462 (July): 391–401. <https://doi.org/10.1016/j.jnucmat.2014.11.066>.
- Haušild, Petr. 2021. “On the Breakdown of the Nix-Gao Model for Indentation Size Effect.” *Philosophical Magazine* 101 (4): 420–34. <https://doi.org/10.1080/14786435.2020.1841916>.
- Heintze, C., F. Bergner, S. Akhmadaliev, and E. Altstadt. 2016. “Ion Irradiation Combined with Nanoindentation as a Screening Test Procedure for Irradiation Hardening.” *Journal of Nuclear Materials* 472 (April): 196–205. <https://doi.org/10.1016/j.jnucmat.2015.07.023>.
- Hosemann, Peter, Daniel Kiener, Yongqiang Wang, and Stuart A. Maloy. 2012. “Issues to Consider Using Nano Indentation on Shallow Ion Beam Irradiated Materials.” *Journal of Nuclear Materials* 425 (1–3): 136–39. <https://doi.org/10.1016/j.jnucmat.2011.11.070>.
- Huang, Y, F Zhang, K Hwang, W Nix, G Pharr, and G Feng. 2006. “A Model of Size Effects in Nano-Indentation.” *Journal of the Mechanics and Physics of Solids* 54 (8): 1668–86. <https://doi.org/10.1016/j.jmps.2006.02.002>.
- Johnson, K.L. 1970. “The Correlation of Indentation Experiments.” *Journal of the Mechanics and Physics of Solids* 18 (2): 115–26. [https://doi.org/10.1016/0022-5096\(70\)90029-3](https://doi.org/10.1016/0022-5096(70)90029-3).
- Kareer, A., A. Prasitthipayong, D. Krumwiede, D.M. Collins, P. Hosemann, and S.G. Roberts. 2018. “An Analytical Method to Extract Irradiation Hardening from Nanoindentation Hardness-Depth Curves.” *Journal of Nuclear Materials* 498 (January): 274–81. <https://doi.org/10.1016/j.jnucmat.2017.10.049>.



	<b>D4.5 Hybrid hardening models from SANS and NI experiments</b>	Page	37/38
		Rev	1
		Date	30/08/2023

- Kasada, Ryuta, Yoshiyuki Takayama, Kiyohiro Yabuuchi, and Akihiko Kimura. 2011. "A New Approach to Evaluate Irradiation Hardening of Ion-Irradiated Ferritic Alloys by Nano-Indentation Techniques." *Fusion Engineering and Design* 86 (9–11): 2658–61. <https://doi.org/10.1016/j.fusengdes.2011.03.073>.
- Liu, Xiangbing, Rongshan Wang, Ai Ren, Jing Jiang, Chaoliang Xu, Ping Huang, Wangjie Qian, Yichu Wu, and Chonghong Zhang. 2014. "Evaluation of Radiation Hardening in Ion-Irradiated Fe Based Alloys by Nanoindentation." *Journal of Nuclear Materials* 444 (1–3): 1–6. <https://doi.org/10.1016/j.jnucmat.2013.09.026>.
- Malerba, L., M.J. Caturla, E. Gaganidze, C. Kaden, M.J. Konstantinović, P. Olsson, C. Robertson, et al. 2021. "Multiscale Modelling for Fusion and Fission Materials: The M4F Project." *Nuclear Materials and Energy*, August, 101051. <https://doi.org/10.1016/j.nme.2021.101051>.
- Mansur, L. K. 1978. "Void Swelling in Metals and Alloys Under Irradiation: An Assessment of the Theory." *Nuclear Technology* 40 (1): 5–34. <https://doi.org/10.13182/NT78-2>.
- Meslin, E., B. Radiguet, and M. Loyer-Prost. 2013. "Radiation-Induced Precipitation in a Ferritic Model Alloy: An Experimental and Theoretical Study." *Acta Materialia* 61 (16): 6246–54. <https://doi.org/10.1016/j.actamat.2013.07.008>.
- Monnet, Ghiath. 2018. "Multiscale Modeling of Irradiation Hardening: Application to Important Nuclear Materials." *Journal of Nuclear Materials* 508: 609–27. <https://doi.org/10.1016/j.jnucmat.2018.06.020>.
- Nanstad, R.K., W.L. Server, M.A. Sokolov, G.R. Odette, and N. Almirall. 2018. "Some useful mechanical property correlations for nuclear reactor pressure vessel steels." Proceedings of the ASME 2018 Pressure Vessel and Piping Conference PVP2018, July 15-20, 2018, Prague, Czech Republic, Paper ID PVP2018-84786.
- Nix, William D., and Huajian Gao. 1998. "Indentation Size Effects in Crystalline Materials: A Law for Strain Gradient Plasticity." *Journal of the Mechanics and Physics of Solids* 46 (3): 411–25. [https://doi.org/10.1016/S0022-5096\(97\)00086-0](https://doi.org/10.1016/S0022-5096(97)00086-0).
- Oliver, W.C., and G.M. Pharr. 1992. "An Improved Technique for Determining Hardness and Elastic Modulus Using Load and Displacement Sensing Indentation Experiments." *Journal of Materials Research* 7 (6): 1564–83. <https://doi.org/10.1557/JMR.1992.1564>.
- Oliver, W.C., and G.M. Pharr. 2004. "Measurement of Hardness and Elastic Modulus by Instrumented Indentation: Advances in Understanding and Refinements to Methodology." *Journal of Materials Research* 19 (1): 3–20. <https://doi.org/10.1557/jmr.2004.19.1.3>.
- Robertson, C., S. Poissonnet, and L. Boulanger. 1998. "Plasticity in Ion-Irradiated Austenitic Stainless Steels." *Journal of Materials Research* 13 (8): 2123–31. <https://doi.org/10.1557/JMR.1998.0297>.
- Röder, F., C. Heintze, S. Pecko, S. Akhmadaliev, F. Bergner, A. Ulbricht, and E. Altstadt. 2018. "Nanoindentation of Ion-Irradiated Reactor Pressure Vessel Steels – Model-Based Interpretation and Comparison with Neutron Irradiation." *Philosophical Magazine* 98 (11): 911–33. <https://doi.org/10.1080/14786435.2018.1425007>.
- Ruiz-Moreno, Ana, and Peter Hähner. 2018. "Indentation Size Effects of Ferritic/Martensitic Steels: A Comparative Experimental and Modelling Study." *Materials & Design* 145: 168–80. <https://doi.org/10.1016/j.matdes.2018.02.064>.
- Ruiz-Moreno, Ana, Peter Hähner, Lukasz Kurpaska, Jacek Jagielski, Philippe Spätig, Michal Trebala, Simo-Pekka Hannula, et al. 2020. "Round Robin into Best Practices for the Determination of Indentation Size Effects." *Nanomaterials* 10 (1): 130. <https://doi.org/10.3390/nano10010130>.



	<b>D4.5 Hybrid hardening models from SANS and NI experiments</b>	Page	38/38
		Rev	1
		Date	30/08/2023

- Saleh, Michael, Zain Zaidi, Mihail Ionescu, Christopher Hurt, Ken Short, John Daniels, Paul Munroe, Lyndon Edwards, and Dhriti Bhattacharyya. 2016. "Relationship between Damage and Hardness Profiles in Ion Irradiated SS316 Using Nanoindentation – Experiments and Modelling." *International Journal of Plasticity* 86: 151–69. <https://doi.org/10.1016/j.ijplas.2016.08.006>.
- Sargent, P.M. "Factors Affecting the Microhardness of Solids, PhD Thesis, University of Cambridge, UK, 1979."
- Seeger, Alfred K. 1958. "On the Theory of Radiation Damage and Radiation Hardening." In *Second United Nations International Conference on The Peaceful Uses of Atomic Energy*, 6:250–73. Geneva, Switzerland: United Nations, New York.
- Soneda, N., K. Dohi, K. Nishida, A. Nomoto, M. Tomimatsu, and H. Matsuzawa. 2009. "Microstructure characterization of RPV materials irradiated to high fluences at high flux." *Journal of ASTM International* 6 (7). <https://doi.org/10.1520/JAI102128>.
- Standard DIN EN ISO 14577-1, Metallic Materials – Instrumented Indentation Test for Hardness and Materials Parameters, 2015.
- Ulbricht, A. 2006. "Untersuchungen an Neutronenbestrahlten Reaktordruckbehälterstählen Mit Neutronen-Kleinwinkelstreuung." PhD Thesis, Freiberg: TU Bergakademie.
- Ulbricht, A., J. Böhmert, and Viehrig, H.-W. 2005. "Microstructural and Mechanical Characterization of Radiation Effects in Model Reactor Pressure Vessel Steels." *Journal of ASTM International* 2 (10).
- Wagner, Arne. 2017. "Long-Term Irradiation Effects on Reactor Pressure Vessel Steels." Halle-Wittenberg: Martin-Luther-Universität.
- Was, G.S., S. Taller, Z. Jiao, A.M. Monterrosa, D. Woodley, D. Jennings, T. Kubley, F. Naab, O. Toader, and E. Uberseder. 2017. "Resolution of the Carbon Contamination Problem in Ion Irradiation Experiments." *Nuclear Instruments and Methods in Physics Research Section B: Beam Interactions with Materials and Atoms* 412: 58–65. <https://doi.org/10.1016/j.nimb.2017.08.039>.
- Xiao, Xiazi, Qianying Chen, Hui Yang, Huiling Duan, and Jianmin Qu. 2017. "A Mechanistic Model for Depth-Dependent Hardness of Ion Irradiated Metals." *Journal of Nuclear Materials* 485: 80–89. <https://doi.org/10.1016/j.jnucmat.2016.12.039>.
- Zhu, Pengcheng, Yajie Zhao, Shradha Agarwal, Jean Henry, and Steven J. Zinkle. 2022. "Toward Accurate Evaluation of Bulk Hardness from Nanoindentation Testing at Low Indent Depths." *Materials & Design* 213: 110317. <https://doi.org/10.1016/j.matdes.2021.110317>.
- Zinkle, S.J., and L.L. Snead. 2018. "Opportunities and Limitations for Ion Beams in Radiation Effects Studies: Bridging Critical Gaps between Charged Particle and Neutron Irradiations." *Scripta Materialia* 143: 154–60. <https://doi.org/10.1016/j.scriptamat.2017.06.041>.
- Zurbuchen, Conrad, Hans-Werner Viehrig, and Frank-Peter Weiss. 2009. "Master Curve and Unified Curve Applicability to Highly Neutron Irradiated Western Type Reactor Pressure Vessel Steels." *Nuclear Engineering and Design* 239 (7): 1246–53. <https://doi.org/10.1016/j.nucengdes.2009.03.008>.

